POLITECNICO DI TORINO
Repository ISTITUZIONALE

Efficient Electromagnetic Modelling of Complex Structures

Publisher copyright

(Article begins on next page)

04 August 2020

POLITECNICO DI TORINO

SCUOLA DI DOTTORATO

Dottorato in Ingegneria Elettronica – XVI ciclo

Tesi di Dottorato

Efficient Electromagnetic Modelling of Complex Structures

Jorge Alberto Tobón Vásquez

Tutore
prof. Giuseppe Vecchi

Coordinatore del corso di dottorato
prof. Ivo Montrosset

Maggio 2014

Contents

Part I

Re-entry vehicle in plasma

Chapter 1

Introduction

1.1 Background and motivations

One of the main challenging issues in the re-entry vehicles communication systems is the communication black-out occurring in the presence of plasma.

Space vehicles re-entering earth's atmosphere produce a shock wave which in turns results in a flow of plasma around the vehicle body. This plasma significantly affects all radio links between the vehicle and ground, since the electron plasma frequency reaches beyond several GHz (figure 1.1).
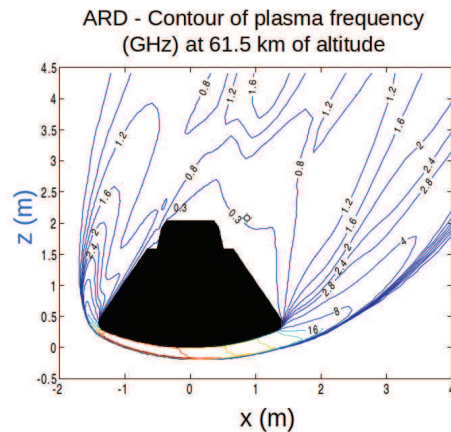

Figure 1.1: ARD - Atmospheric Re-entry Demonstrator

While the presence of relay satellites in geostationary orbit avoids the total black-out experienced in early space flights, many times space vehicles are required to communicate directly with ground based stations (fig. 1.2). The warmest and

densest part of the plasma is oriented to earth (shock-wave in atmosphere) and the signal blockage in that direction is higher.
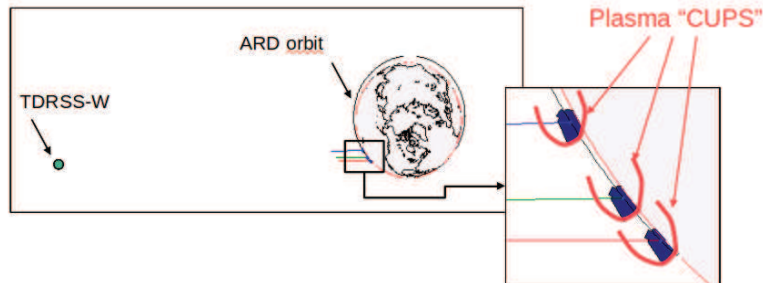
Figure 1.2: Vehicle-plasma system links.

In this work, a model of the propagation in plasma issue is developed. The radiofrequency propagation from/to antennae installed aboard the vehicle to the ground stations (or Data Relay Satellites) can be predicted, and the position of this antennae improved before a mission launch.

The plasma variation in time (due to its natural behaviour and to the mission trajectory) is slow respect the electromagnetic field variation in the radio wave propagation, it permits to use time "snapshots" in which plasma is considered constant while solving the wave propagation in its interior. In the range of operative frequencies in the space communication and with the expected densities of plasma, it can be considered as an inhomogeneous dielectric, with propagation and cut-off regions.

1.2   Recent studies

The ESA Atmospheric Re-entry Demonstrator (ARD) program investigated experimentally the link to NASA TDRSS satellite. Pre-flight (1996) and post-flight (2001) studies for the S-band link predicted that propagation through plasma would involve attenuations higher than 100dB in obstructed directions. ARD flight measurements showed much lower link attenuation (Table 1.1).

2D Ray Tracing

In 2004, Vecchi et al. [2,3] proposed the difraction of signals inside the plasma as a better solution. Instead of study the plane-wave straight link direction attenuation, case in which thick cutoff layers are thus crossed and high attenuation expected, the

Altitude (km)	Prediction 1996	Calculated 2001	Measured 1998
85	> 200dB	140 dB	12 dB
61.5	-	200 dB	21 dB
45	0 dB	0 dB	4 dB

Table 1.1: Direct link attenuation.

multi-path phenomena inside the plasma cup is considered. The diffraction from the blocking plasma rim permits the signal to arrive to the receiver also if direct link blocking is present (fig. 1.3). A model based on these considerations should be more accurate.
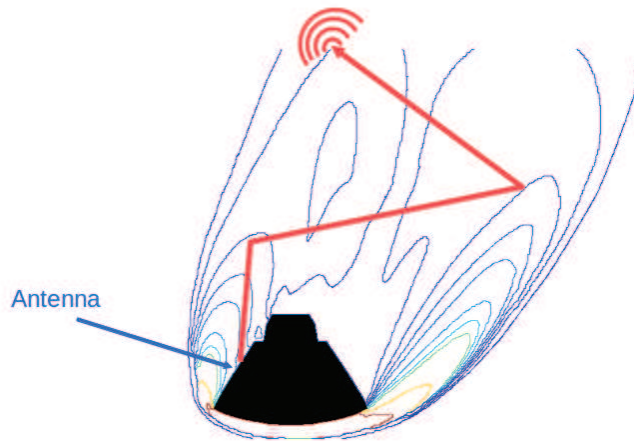
Figure 1.3: Difraction in 2D case.

The strategy in that case was focused on a 2D case, so only the cut in the link plane was considered. A ray tracing approach was used inside the plasma region, from antenna to free space, as figure 1.4 depicts. The plasma region is surrounded by free-space, so free-space radiation can be used to obtain the field everywhere, from the equivalent (Huygens) sources defined on the boundary between plasma and free-space.

Altitude (km)	Calculated 2D model	Measured 1998
85	14 dB	12 dB
61.5	14.6 dB	21 dB
45	3.8 dB	4 dB

Table 1.2: 2D ray tracing vs. measures.

Table 1.2 confirms that the diffraction approach is closer to the measured data
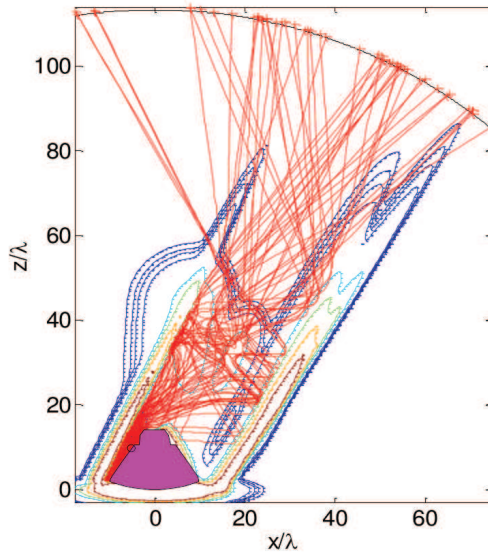
Figure 1.4: Ray tracing in 2D

that the direct-link estimations done before. A 3D extension of the strategy, using realistic plasma data, will give more accurate results and a more flexible predicition tool. The development of that tool is the goal of the present work.

1.3 Present work strategy

To solve a plasma-vehicle propagation problem a 3D ray tracing is proposed, in addition to the field equivalence principle. The vehicle-plasma system is substituted by equivalent currents on its boundary (surface in the 3D case), radiating in free space; the fields on the boundary are obtained by solving the propagation from the antenna (on the spaceship) up to the plasma boundary.

The formation of the re-entry plasma is related to the kinematics and shape of each particular case, the electromagnetic model proposed here will be directly derived in each case from the output data of Computational Fluid Dynamics simulations.

The complete model developed in the following is collected as a single tool that allows the characterization of the communication channel based on the plasma information, the antenna position and features and geometry of the spaceship. The characterization of the channel permits the calculation of BER (Bit Error Rate) and FER (Frame Error Rate) of the received signal in the communication point of view.

Chapter 2

Objectives

The analyzes aimed at evaluating the radiation pattern of the antennae installed aboard the re-entry vehicle are wanted. This research activity has as main objective the development of a simulation environment for the prediction of the radiation performance of antennas mounted on re-entry spacecraft and plasma distributed around it.

The developed EM (electromagnetic) tool must be in grade of guide the system engineer in the specification and assessment of the communication system's architecture, providing non interfering, continuous communication under all flight conditions with special attention to the communications blackout phase.

The available electromagnetic models of the antenna radiation in presence of the plasma shroud shall be consolidated and shall be further developed to become suitable for more general vehicle geometries and antenna types.

The simulation program will allow the modeling of the communication channel, depending on the antenna location, re-entry vehicle geometry and plasma situation.

To achieve this main goal a set of specific objectives must be solved:

- Correct modelling of the plasma cloud that is generated around the re-entry vehicle.

- Study of the vehicle interaction with the propagation fields.

- Calculation of the field in any point of the space, from the antenna in the plasma-vechicle system.

- Definition of the approximation used to solve the propagation in plasma issue.

- Appropriate set of validation simulation for each stage and for the complete tool.

As starting point to the design of this simulation tool, two physical data are available and these information will be considered as the input, the base of the subsequent work.

The plasma information will be obtained from Computed Fluid Dynamics (CFD) simulations, and will contain the main information of the plasma characteristics. This information will be used in the plasma modelling.

The vehicle geometry information is needed to study the electromagnetic signal and vehicle interaction. The geometry should be the used in the CFD simulation, ensuring consistency between the two main input data.

The following chapters will describe how a reliable simulation tool, that predicts the behaviour of certain antenna-plasma configuration starting from the vehicle and CFD characteristics, is builded and tested.
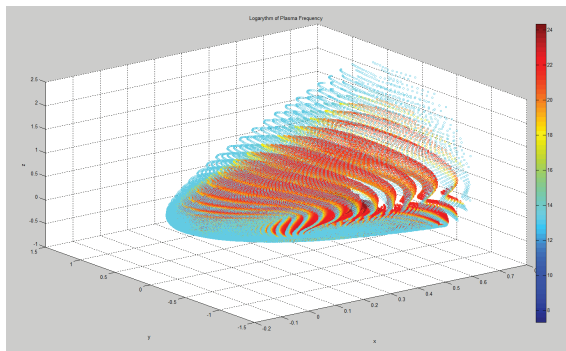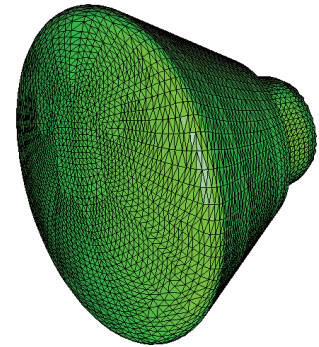
(a) IXV Mach 25 log plasma freq
(b) ARD Re-entry vehicle

Figure 2.1: Inputs of developed EM tools

Chapter 3

EM Formulation

In this chapter the electromagnetic formulation of the problem is presented. The development of the tool is based in the next aspects, and in their interaction. Further information of each one is presented in the sections of this chapter.

- **Plasma medium modeling:**
  The plasma is considered as stationary, multiple analyses at different instants are used. Linearity of the system is assumed, and the plasma body is modeled as an inhomogeneous dielectric body. The permittivity is computed from the electron plasma frequency, the collision plasma frequency and the link frequency.

- **Equivalence theorem:**
  Equivalence principle is used to remove the plasma medium and place equivalent (electric and magnetic) currents/fields on the plasma boundary. To compute these equivalent currents/fields on the plasma boundary the **Eikonal (HF) approximation** is used inside the plasma. In other words: Ray Tracing approach is used to transport field information from source to the plasma boundary through the plasma body.

- **Re-entry vehicle interaction:**
  The vehicle geometry is modeled via a patch triangular surface mesh. The interaction between field and vechicle is modeled with the reflection of rays on the local tangent plane.

- **Radiation from equivalent surface:**
  Exact radiation of equivalent currents in vacuum yields the scattered field on the infinite space, having in this way into account the effect of plasma in the final solution.

Figure 3.1 summarizes the main steps explained before: An equivalent surface is defined where the equivalent currents are computed from the plasma-vehicle interior model (fig 3.1a), the scattered field is obtained from the equivalent surface (fig 3.1b).
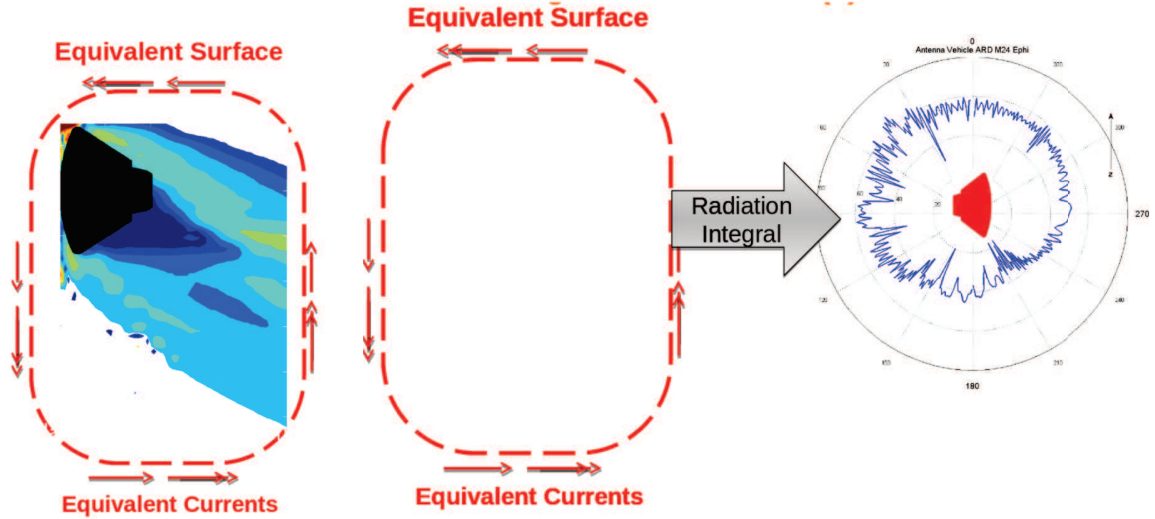
(a) Plasma system to equivalence surface.

(b) Equivalence surface to scattered field.

Figure 3.1: General scheme of proposed tool.

3.1 Plasma medium modeling

Plasma is a state of matter similar to gas in which a certain portion of the particles is ionized: it is an electrically neutral medium made up of positive and negative particles (the overall charge of a plasma is roughly zero). Plasma is formed when gas temperatures are elevated, as in the case of the air around re-entry vehicles.

Since the formation of the re-entry plasma critically depends on the re-entry vehicle shape and kinematics, the related model has been directly derived from the output data of the Computational Fluid Dynamics simulations.

Plasma characterization

A plasma cloud may be characterized using two properties: Plasma Frequency and Collision Frequency. The Plasma Frequency measures plasma oscillations of the electrons and the Collision Frequency measures the frequency of collisions between

electron and neutral particles. For electromagnetic interaction the plasma is modelled as a non-homogeneus dielectric medium at an analysis frequency f.

Equation 3.1 shows the relation used to compute permittivity information (ϵ_r) from the link frequency, plasma frequency and collision frequency (f,f_p and f_c)

$$\epsilon_r(x,y,z) = n^2(x,y,z) = 1 + \frac{f_p^2(x,y,z)}{f(jf_c^2(x,y,z) - f)} \tag{3.1}$$

Usually the electron plasma frequency is large compared to the electron - neutral collision frequency. When this condition is valid, electrostatic interactions dominate over the processes of ordinary gas kinetics and the relative permittivity becomes equation 3.2

$$\epsilon_r(x,y,z) = n^2(x,y,z) = 1 - \frac{f_p^2(x,y,z)}{f^2} \tag{3.2}$$

CFD input file

CFD solutions are a collection of data concerning plasma environment around the vehicle. Much information is available and most of it is not useful to derive the electron plasma model of interest. Data were computed during CFD simulations for a given number of points around the vehicle. Usually, each point is part of a structured mesh. CFD solution files store therefore a set of parameters stating point position, mesh information and plasma information. The number of parameters for each CFD solution can vary according to the adopted gas mixture (number of species). The list of parameters and their order is reported at the beginning of each CFD solution file, an example of parameters collection is reported in table 3.1.

Name	Parameter
Nparam	Number of parameters for each mesh point.
xpos	x-coordinate of simulated point.
ypos	y-coordinate of simulated point.
zpos	z-coordinate of simulated point.
cEpos	electron mass density.
telpos	electron temperature.
tpos	gas mixture temperature.
rhopos	fluid density.
ppos	gas pressure

Table 3.1: CFD simulation parameters.

The values of Plasma Frequency and Collision Frequency can be obtained from the previous parameters as showed in equations 3.3 and 3.4, where the constants are $f_{cc} = 5.029 \times 10^6$ and $f_{pc} = 8.985\sqrt{\frac{6.022045 \times 10^2 6}{5.4858 \times 10^{-4}}}$. The notation is the same used in table 3.1.

$$f_p = f_{pc}\sqrt{cEpos \cdot rhopos} \tag{3.3}$$

$$f_c = f_{cc} \cdot ppos\sqrt{telpos \cdot tpos} \tag{3.4}$$

Figure 3.2 shows plasma information visualized from a CFD data file. The figure 3.2a shows the original frequency plasma cloud, and figures 3.2b and 3.2c show the relationship between plasma frequency and permittivity in 2D cuts (for easy visualization).

(a) 3D - Plasma Frequency (b) 2D - Plasma freq. (c) 2D - Permittivity

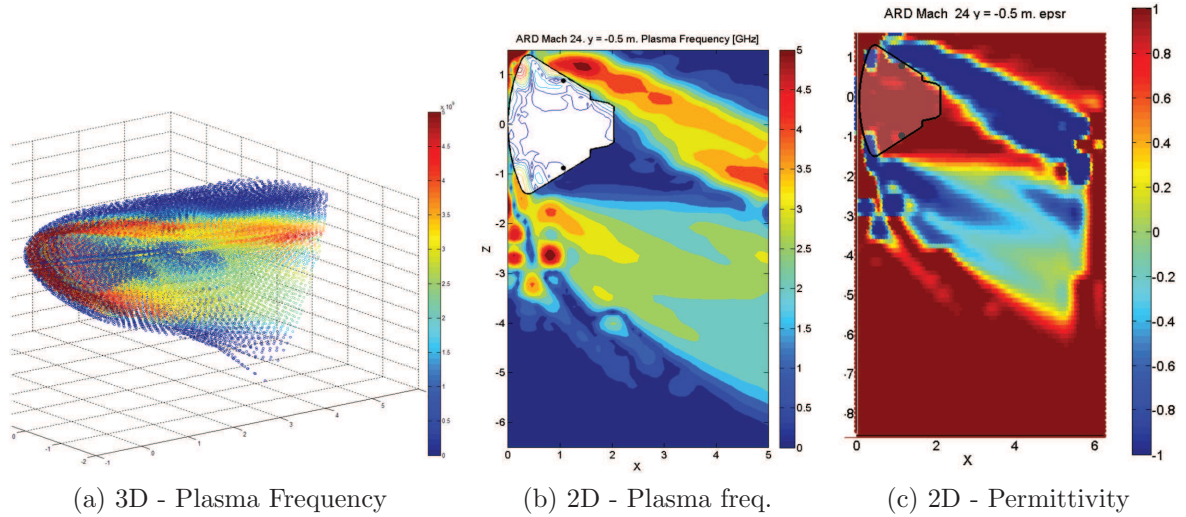Figure 3.2: Plasma info from CFD simulation

3D interpolation

Since the plasma density data are known only at a cloud of points, a specialized 3D interpolation scheme is implemented to have information of the plasma body in any point inside the surface of interest. The interpolation has been implemented in order to avoid any oscillation between nodes that induces large artifacts in ray propagation.

Figure 3.3 shows how the 3D interpolation permits to calculate the permittivity values in arbitrary points as in 3.3b, starting from a cloud that is defined by the CFD simulations (fig. 3.3a).

In this case a spline interpolation has been used. Spline interpolation is preferred over polynomial interpolation because the interpolation error can be made small even when using low degree polynomials for the spline. Spline interpolation avoids the problem of Runge's phenomena, which occurs when interpolate with high-degree.

(a) CFD simulations   (b) 3D interpolation
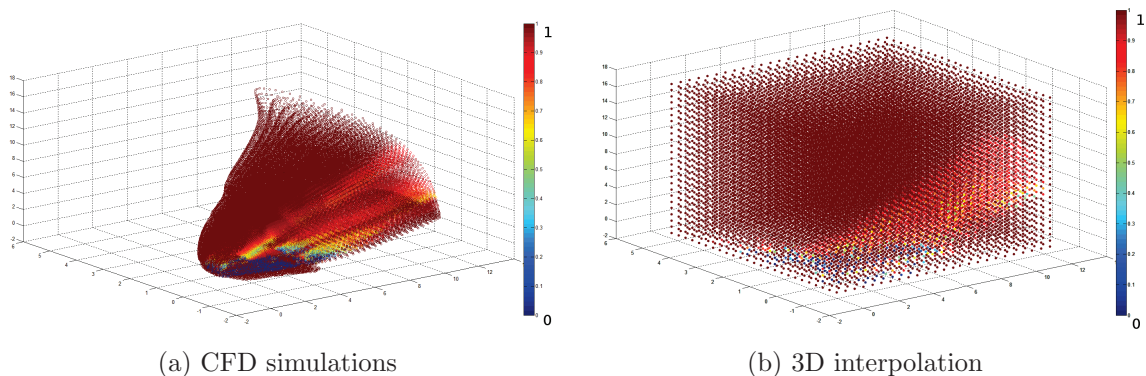
Figure 3.3: dielectric constant ϵ_r (real part)

3.2   Propagation in Plasma

To solve the propagation in plasma problem, applicable modelling strategies are in general limited to:

- Ray-based methods that approximate the propagation in the plasma region via the Eikonal Ansatz. The radiation of the so-computed fields just outside the plasma region is then carried out exactly (Radiation Integral)

- Full-wave techniques, i.e. addressing the numerical solution of Maxwell equations without approximations (such as FDTD, FDFD, FEM).

All of these strategies are able to manage in-homogeneous dielectric volumes (as the plasma cloud has been modelled), that is the core of the tool under development. Ray based techniques are intrinsically well suited to analyze electrically large problems, as usually required for the problems of interest. As any asymptotic technique it starts from an equivalent antenna free-space radiation model (e.g. Huygens sources, pattern, etc.) and allows to effectively managing propagation along the plasma cloud

and reflection on vehicle surfaces.

Full-wave methods for this problem are in practice limited to the technique called FDTD (finite-difference time-domain), since computational costs are lowest especially in term of memory requirements. Being a time-domain method, handling of the dispersive properties of the plasma is required, but this is standard. The drawbacks are especially in the computational load, but care must be exercised with two well-known critical issues: numerical dispersion and stability. The first issue is a common feature of all explicit time-domain (differential) methods; it manifests itself into errors in phase (propagation), thus especially relevant for electrically large regions (as of interest here). Its bounds for homogeneous media are expected to be exceeded in strongly non-homogeneous media as those of present interest. Stability imposes constraints on spatial and temporal discretization, often resulting in larger problems than expected only on the basis of time scales (and maximum frequency). In addition, negative values of permittivity require extra care and resources (while customarily addressed).

Ray tracing approach is chosen to model the propagation in plasma. The method results in a numerically efficient tool. Each ray is independent and uncoupled respect the other rays, the tool can be easily parallelized and the complexity scale lineary.

Ray Trajectory

The propagation of a ray field inside the inhomogeneous dielectric body, including the ray trajectories and the phase, amplitude and polarization, is considered.

Each ray has associated in the moment of been shot a field that is the sampling of a source. The far field pattern of an antenna can be used as initial field of a set of shot rays.

Ray trajectory is obtained inside the plasma by solving Eikonal Equation. So the curvature of ray at each point is proportional to the gradient (variation) of the dielectric constant (ϵ_r).

In the first order of Lunenburg - Kline series approximation, the fields are being expressed through:

$$E(r) \approx E_0(r)e^{-jk_0 S(r)} \tag{3.5}$$

and

$$H(r) \approx H_0(r)e^{-jk_0 S(r)} \tag{3.6}$$

13

where E_0, H_0 and S are assumed to be slowly varying over one (local) wavelength $\lambda = \lambda_0/n$. This translates into the same requirement for the medium parameters, that in turn can be stated as the condition

$$\lambda \nabla |log(n)| \ll 1 \tag{3.7}$$

Of course this translates into a smoothness hypothesis on the shape of plasma density profiles, at least in the region of interest for radiation.

Insertion of Lunenburg - Kline approximation into Maxwell equations, together with the slow variation assumption, yield the Eikonal equation:

$$\nabla |S| = n \tag{3.8}$$

for the Eikonal normalized phase S whose solution, upon specification of an initial phase front, provides the ray trajectories. In other words, the numerical solution of the Eikonal equation is formulated in terms of equations for the characteristic curves, involving the normalized local wavevector $\xi = \nabla |S|$, and the position r along the ray itself. Using the arc-length w along the ray, the characteristics method results in solving the following system of ordinary differential equations (ODE):

$$\begin{cases} \dfrac{dr_i}{dw} &= \dfrac{\xi_i}{n^2} \\ \dfrac{d\xi_i}{dw} &= \dfrac{1}{2n^2}\dfrac{\partial n^2}{\partial r_i} \end{cases} \tag{3.9}$$

The equation above provided the position vector r (see fig.3.4), where w is the electrical length and s is the geometrical lenght, $i = 1,2,3$, $\xi_i = n\hat{t}$ and $\epsilon_r = n^2$.
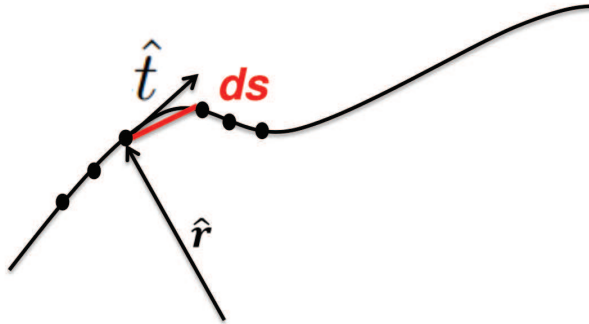

Figure 3.4: Ray trajectory

When the ray trajectory is calculated the phase can be computed by Fermat's pinciple, using the optical path length (equation 3.10)

$$\phi = \frac{2\pi}{\lambda_0} \int_{s_{in}}^{s_{fin}} n(\mathbf{r}(s))ds \qquad (3.10)$$

Field Polarization is evaluated according to the ray curvature (see fig. 3.5). The polarization vector e_2 , at P_2, is related to the polarization vector e_1 at P_1, by the equation:
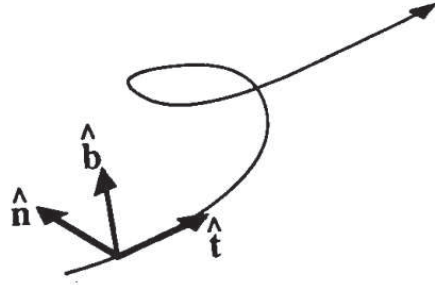

Figure 3.5: Normal, binormal and tangent vector. $\hat{n} = \frac{\hat{t}'}{|\hat{t}'|}$ and $\hat{b} = \hat{t} \times \hat{n}$

$$\hat{e_2} = \hat{n_2} \cos(\theta_0 - \theta) + \hat{b_2} \sin(\theta_0 - \theta) \qquad (3.11)$$

where

$$\theta_0 = \tan^{-1}(\frac{\beta_0}{\alpha_0}), \quad \theta = \int_{P_1}^{P2} \tau ds$$

$$\tau = \frac{(\hat{t} \times \hat{t}') \cdot \hat{t}''}{|\hat{t} \times \hat{t}'|^2}, \quad \hat{e_1} = \hat{n_2}\alpha_0 + \hat{b_2}\beta_0$$

where $\hat{n}$, $\hat{b}$ and $\hat{t}$ are the normal, binormal and tangent vectors and τ is the ray torsion.

An obvious violation of the Eikonal Ansatz happens at cut-off (resonance) layers, where n^2 vanishes and undergoes a sign change. In this situation, or in its close proximity, the solution of a local canonical problem has to be employed, that allows to treat this situation as a localized reflection (tunneling across the cut-off layer is not such as to provide significant propagation). In practice, however, this situation is rarely encountered, because resonance is it typically located at high-density boundary layers with fast variations of densities, with associated sharp bending (the ray radius of curvature is proportional to the gradient of n); therefore, only if the ray

arrives almost parallel to this density gradient the cutoff condition is encountered. Before analyzing the impact of this, it is important to stress that fast variations of density (and the associated large acceleration along ray trajectories) are indeed a cause of violation of the Eikonal Ansatz, causing the field to be poorly represented at these locations; however, this is not the case when observing the field away from these critical points (think of the geometrical optics approximation of fields in focusing systems like reflectors and lenses).

Tube propagation

The way to recover the fields amplitudes is by using power conservation arguments along a ray tube. A ray tube is a family of characteristic curves that evolves in space according to the equations above. Hence, if the power density is known at the ray launch point (boundary conditions surface), local amplitude along the ray tube is found from the local aperture of the tube (spread factor) (fig. 3.6). The advantage of using a ray tube formulation resides in its robustness in the presence of caustics.

$$|E(w_2)|=|E(w_1)|\sqrt{\frac{A_1}{A_2}} \tag{3.12}$$

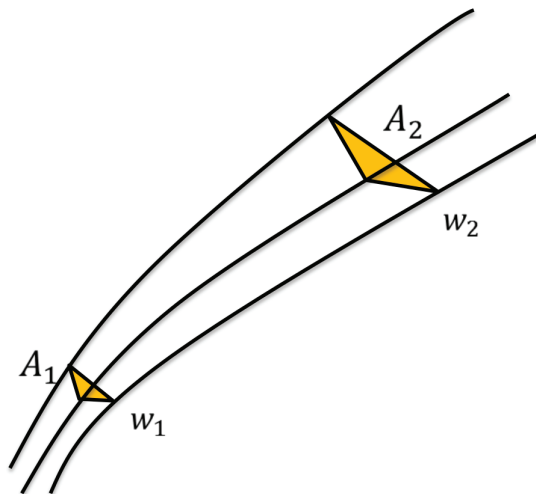Figure 3.6: Tube propagation

## 3.3   Vehicle interaction

The vehicle is assumed to be a Perfect Electric Conductive (PEC) surface and is approximated using a triangular facet mesh. This kind of mesh is broadly used

because its flexibility, easiness in the storage and management, and mainly because can describe correctly curved and detailed bodies.

The surface mesh is generated directly from the surface points extracted from the CFD data, ensuring the match between plasma and vehicle data. The points in figure 3.7a are used to obtain a triangular mesh (fig. 3.7b) trough Delaunay triangulation.
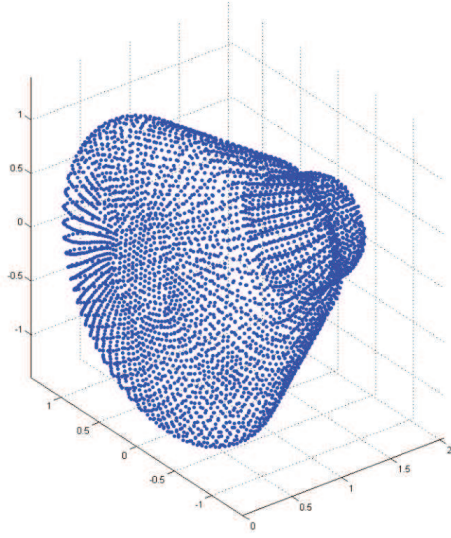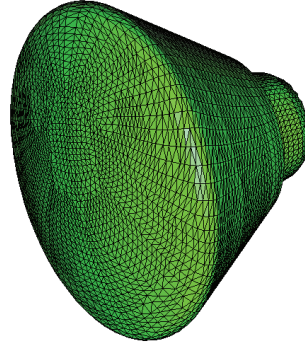
(a) Vehicle points   (b) Vehicle Mesh

During the ray tracing process, the trajectory is checked to understand if a particular ray finds the vehicle surface. When a ray hits the surface, a two-step algorithm is applied to perform the reflection:

- The ray is stopped when it crosses the vehicle surface ant the intersection point is found.

- The ray is re-shot from the ray-triangle intersection point. The new direction and polarization are defined by local reflection on local tangent PEC plane (usual ray reflection).

The reflections is depicted in figure 3.7 in an arbitrary surface case.

The curvature of the surface should be considered in a simple ray tracing case, because the reflection of a ray in a curve body depends on the curvature around the point of bouncing. In this case the electromagnetic wave is not related to a single
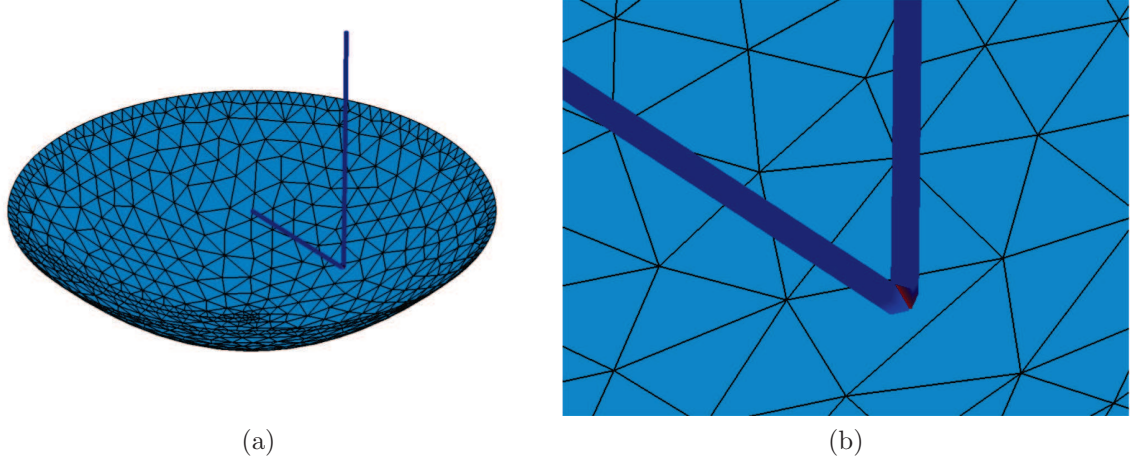
(a)　　　　　　　　　　　　　(b)

Figure 3.7: Reflection on metallic structure

ray, but to a propagation tube. The effect of the curvature on the wave propagation is considered by the spread of the propagation tube whent it hits the surface. The curvature of the surface is appropriately described by the triangular mesh.

3.4　Equivalence surface

The equivalent surface on the plasma boundary (or in a canonical surface that encloses it) will be a virtual surface where equivalent currents/fields are computed from the plasma-vehicle system to use them as source in the calculation of scattered field in free-space.

This equivalent surface is the result of the intersection of the propagation tubes (presented in section 3.2) and an arbitrary but convenient surface that encloses the plasma. The more convenient arbitrary surface would be the plasma boundary, but to find easier the tube-surface intersection a canonical surface (cylinder, sphere, i.e.) is proposed. The canonical surface adds some free space propagation of the rays, but considering the dimensions and the behaviour of rays in the complex system, this extra ray tracing is not considered a problem.

The tubes have a triangular section, so the intersection with the arbitrary surface will be described by triangular patches as showed in figure 3.8a. Figure 3.8b shows an example of equivalent fields in a particular case (dipole parallel to cylinder axis in free-space).

In a realistic case, the plasma tends to focus the rays in some region. Some rays might be stopped because are trapped inside a region of the plasma. These conditions create an equivalent surface that is not close as the one presented before, but open and even with triangle superposition as shown in figure 3.8c. This equivalent surface is considered valid, because reflects how the energy of the electromagnetic wave is propagated inside the plasma. The triangles in superposition are considered in the following radiation as independent sources, and their effects on the scattered field added, due to the linearity of the free-space propagation.

(a) Equivalent surface. Free-Space

(b) Equivalent currents.

(c) Equivalent surface. Plasma-vehicle
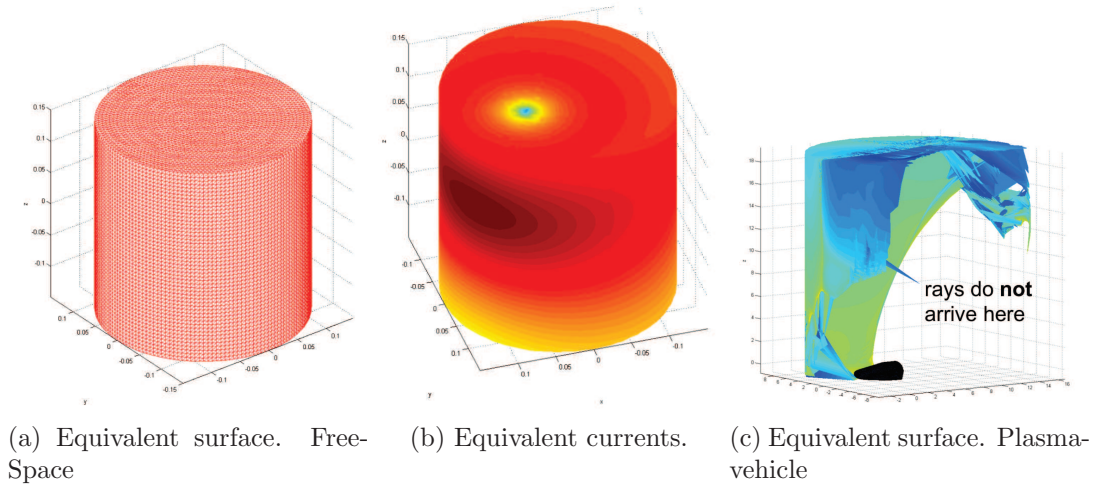
Figure 3.8: Equivalent surface.

As the amplitude of the propagated field in the tube stage is associated to the triangle area (flux conservation), the equivalent amplitude field on the equivalent surface is related to the triangular patches, not to the vertices. The polarization and phase information, instead, is related to each ray; an average of these values (3 vertices in each tube) is considered and assigned to each triangle.

Radiation from equivalent surface

Once the total equivalent current/fields are calculated on an arbitrary equivalent surface, the scattered field in the exterior region can be calculated. The equivalent sources radiate in free space to give rise to the scattered field. The scattered far field can be calculated using the following radiation integral:

$$\mathbf{E_s} = \frac{e^{-jk_0 r}}{r}[\hat{\theta}A_\theta + \hat{\phi}A_\phi] \tag{3.13}$$

where

$$\begin{bmatrix} A_\theta \\ A_\phi \end{bmatrix} = \frac{jk_0}{4\pi} \int_{\texttt{EqSurface}} e^{-j\vec{k_0}\cdot\vec{r'}} \cdot \left(\begin{bmatrix} -\hat{\phi} \\ \hat{\theta} \end{bmatrix} \times \mathbf{E}(\mathbf{r'}) + Z_0 \begin{bmatrix} -\hat{\phi} \\ \hat{\theta} \end{bmatrix} \times \mathbf{H}(\mathbf{r'}) \right) \cdot \hat{\mathbf{n}} ds' \quad (3.14)$$

where $\hat{\theta}$, $\hat{\phi}$ are the unit vectors in the directions θ, ϕ and $\hat{k}_0$ is the direction vector which points from the origin to the observation point with magnitude k_0.

As the information on the equivalent surface is available on the triangular patches, some modifications can be done to the radiation integral, obtaining a tube integration scheme. The total equivalent surface can be considered as the superposition of small tubes, the contribution of each tube is calculated separately, parallelization can be considered because each tube is independent.

In our case, the equivalent surface is a collection of triangle patches, on each triangle the field has constant magnitude and linear phase variation. The contribution of each triangle on the equivalent surface is determined by

$$\begin{bmatrix} A_\theta \\ A_\phi \end{bmatrix}_i \cong \frac{jk_0}{4\pi} e^{-j\vec{k_0}\cdot\vec{r_i}} \cdot \left(\begin{bmatrix} -\hat{\phi} \\ \hat{\theta} \end{bmatrix} \times \mathbf{E}(\mathbf{r_i}) + Z_0 \begin{bmatrix} -\hat{\phi} \\ \hat{\theta} \end{bmatrix} \times \mathbf{H}(\mathbf{r_i}) \right) \cdot \hat{\mathbf{n}}(\Delta A) S(\theta, \phi) \quad (3.15)$$

where

$$S(\theta, \phi) = \frac{1}{\Delta A} \int_{\texttt{TrianglePatch}} e^{-jk_0(\vec{k_0}-\hat{t})\cdot(\vec{r'}-\vec{r_i})} dS' \quad (3.16)$$

and r_i is the position vector of the triangle barycenter, r' the position vector of the points on the triangle, $\hat{\mathbf{n}}$ is the normal to the triangle surface and $\hat{t}$ is the direction of propagation of the equivalent field ($\mathbf{E} \times \mathbf{H}$).

The total scatter field is a superpostion of the scattered field of all the triangles on the equivalent surface:

$$\begin{bmatrix} A_\theta \\ A_\phi \end{bmatrix} = \sum_i \begin{bmatrix} A_\theta \\ A_\phi \end{bmatrix}_i \quad (3.17)$$

The radiation scheme presented here is based on the proposed by Kim in [4].

Chapter 4

Algorithm Overview

For the implementation of the Propagation in Plasma tool, Fortran language has been used. Fortran is used for scientific/numerical computing because its good performance in parallelization, portability, matrices and array management and high efficiency.

The present chapter gives a language-independent overview to the implemented algorithm. The inputs and set up are briefly discussed, and the ray tracing core is explained step by step.

4.1   General algorithm

The program is divided in two main blocks, as could be deduced from the formulation, and as is depicted in figure 4.1. The ray tracer part performs the ray propagation from the source until the equivalent surface, while the field radiation block takes the equivalent field to compute the scattered field. Each block has its needed and produced information as will be explained in the following.

Is possible to use each block separately and save data to be reused. For example, the equivalent currents can be loaded by the second block to obtain scattered fields, without the need of make the ray tracing each time.

Inputs

In previous chapters has been said that the only two inputs of the simulator were the CFD file (plasma information) and vehicle geometry. To these inputs we must add some information for the setting up of the electromagnetic model. The link frequency is neede for the plasma modeling (first block) and for the electromagnetic
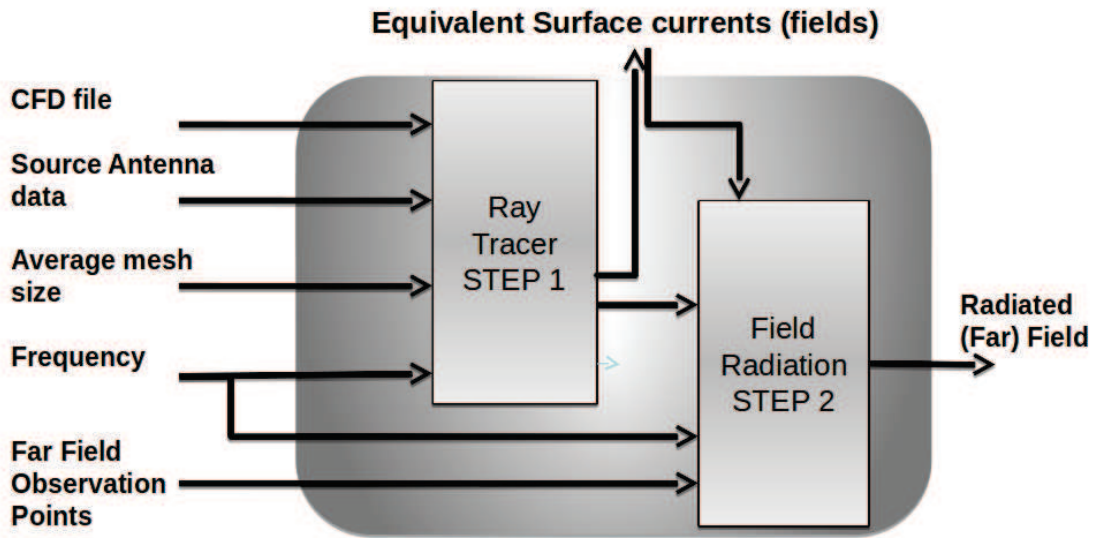
Figure 4.1: General algorithm overview

propagation (both blocks). The position of the antenna on the spaceship and its radiation pattern are needed to the initialization of the rays, as the quantity of rays.

The second block needs the equivalent currents (as external input or as result of previous block) and the points where scattered field is wanted.

Intermediate data

The equivalent surface and the equivalent currents (fields) on it can be saved in a external file, used then to visualize where the energy concentrates or as input of the second block.

Output

The ouput of the simulator is the scattered field on the indicated points. This information together with the free-space field case is useful to the characterization of the channel.

4.2   Workflow

In this section the sequence of steps followed in a generic simulation case is vriefly explained. Figure 10.3 shows the workflow from the input data reading until the

scattered computation in the radiation integral. The CFD plasma reading includes the removal of extra information (as explained in section 3.1) as the elimination of redundant data (repeated points i.e.), this is necessary to have a good interpolation in subsequent steps of the algorithm. The CFD files are also big files, the management can be heavy if no needed information is held. On the following step the vehicle geometry is obtained from the data points (Delaunay triangulation) and the plasma model is computed from the plasma and collision frequency, and then interpolated.

Rays initialization creates and shoot the rays. The quantity of rays is determined by a set up parameter, and to each tube (defined by 3 rays) the source field is assigned (antenna pattern).

After the ray tracing inside the plasma cloud (explained in next section), the equivalent surface is builded. The equivalent surface is the intersection of the propagation tubes and a arbitrary surface. In this case a canonical surface is used, doing easier to check when the tub exits the surface.

With the equivalent surface and equivalent currents computed, the radiation is done according to section 3.4.
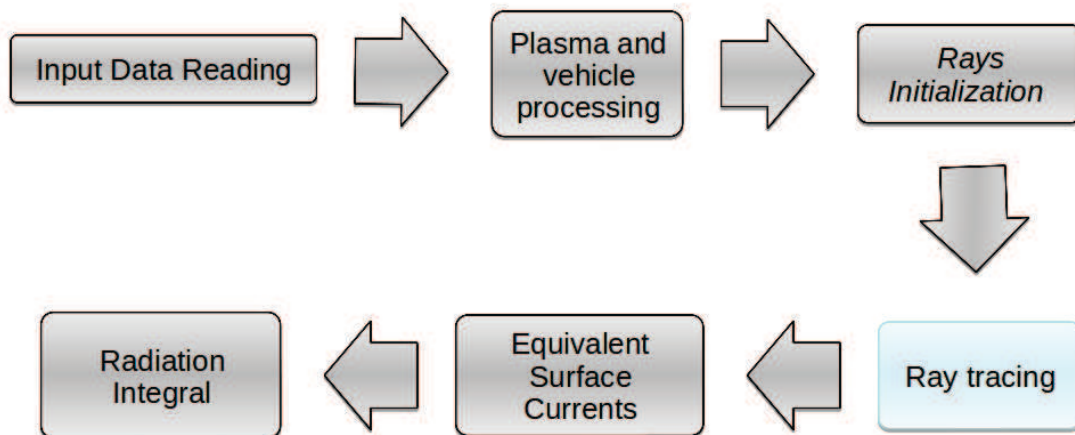

Figure 4.2: Program workflow

4.3   Ray tracing algorithm

The core of the simulator is certainly the ray tracing propagation (together wit the tube propagation assumption): the way to model the propagation inside the plasma-vehicle system to obtain the equivalent fields on the equivalent surface.

The ray tracing process follows the workflow depicted on figure 4.3. This algorithm is defined for the ray trajectories (the field amplitude information is related to tubes, and phase and polarization are related to the trajectory itself).

After the initialization of the ray (that includes the definition of tubes and the initial field assignment) each ray is shot. Each ray is independent, which makes the ray trajectory calculation highly parallelizable.

The Ordinary Differential Equations (ODE) system resulted from the Eikonal equation (section 3.2, equation 3.9) is solved in each step using a Runge-Kutta method (RK4). After obtaining each new trajectory point two checks are needed: the first to see if the ray has found the vehicle surface, the second to indicate the exiting from the equivalent surface.

If the ray has found the vehicle surface, a new initial values are given to the ray, that will be reshoot from a new point, and the ray trajectory calculation follows as usual, but considering the new source point. In the case of exiting the equivalent surface the ray is stopped and the information related to it saved to the subsequent calculation of the equivalent fields.
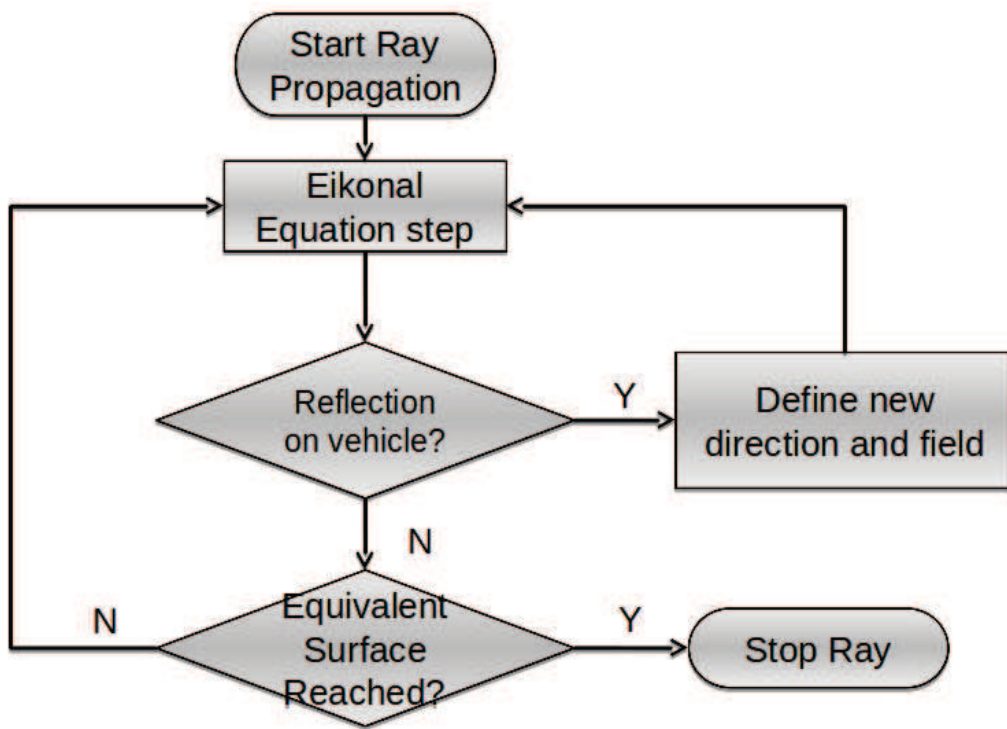
Figure 4.3: Ray tracing workflow

Chapter 5

Validation

In this chapter we report a set of simulations to validate the EM (electromagnetic) solver used to test the propagation in plasma tool.

The section *Ray Trajectory* is focused on the visual evaluation of the ray trajectories (first part of the simulation process). A ray will be curved with the variation of dielectric properties, the behaviour is known in some lens used as reference.

In section *Scattered Field* extends the use of the tool to a second stage. The field scattered for a dielectric body is related to the correct trajectory but also to the radiaton part from the equivalent surface to any point in the space.

The following part is about the presence of a metallic object, in this case a reentry vehicle. The rays bounce on the metallic surface and the scattered field is compared with MoM-bases simulations.

5.1 Ray trajectory

The first validation is related to the correct description of the trajectory in a given medium.

Maxwell's Fisheye

The Maxwells fisheye is a spherical symmetric medium with dielectric constant given by:

$$\epsilon_r = \frac{4}{\left(1 + \left(\frac{r}{R}\right)^2\right)^2} \tag{5.1}$$

this ϵ_r profile is indicated in figure .
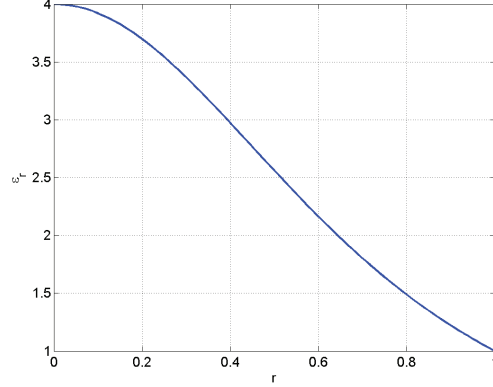

Figure 5.1: ϵ_r profile for a Maxwells Fisheye.

The medium has dielectric constant equal to 1 at r = R, and has the property that rays crossing the sphere at the point $r_1 < R$ are directed to the antipodal location on the same sphere of radius R1.
The source has been positioned into the sphere as in figure , and in the figure is possible to observe how any ray that departs from a point (where the antenna is located) will arrive to the antipodal point.

The ϵ_r values have been interpolated from a cloud that samples a continuous dielectric profile. The cloud information must be loaded instead the plasma file as input for the EM tool.

Luneburg lens

Luneburg lens is a spherically symmetrical lens with the following dielectric profile

$$\epsilon_r = \begin{cases} 2 - \left(\dfrac{r}{R}\right)^2 & \text{if } r \leq R \\ 1 & \text{if } r > R \end{cases} \tag{5.2}$$

where R is the radius of the lens as shown in figure 5.3 . This lens has the appealing characteristic that, when a plane wave impinges upon (a hemisphere of) it, all the energy collected by the lens is focused to the baricenter (pole) of the opposite hemisphere. Conversely, waves produced by a source located on the surface of the lens are collimated such that a plane wave front results at the opposite side.

The simulation has been made in the first case as shown in figure 5.4a: plane wave that is focused in a point as is possible to observe in figure 5.4. The lens dielectric values are loaded instead of plasma information.

freq. = 1 GHz
R = 1 m

source: short
electric dipole

equivalent surface

(a) Simulation scheme

antipodal location

source: short
electric dipole
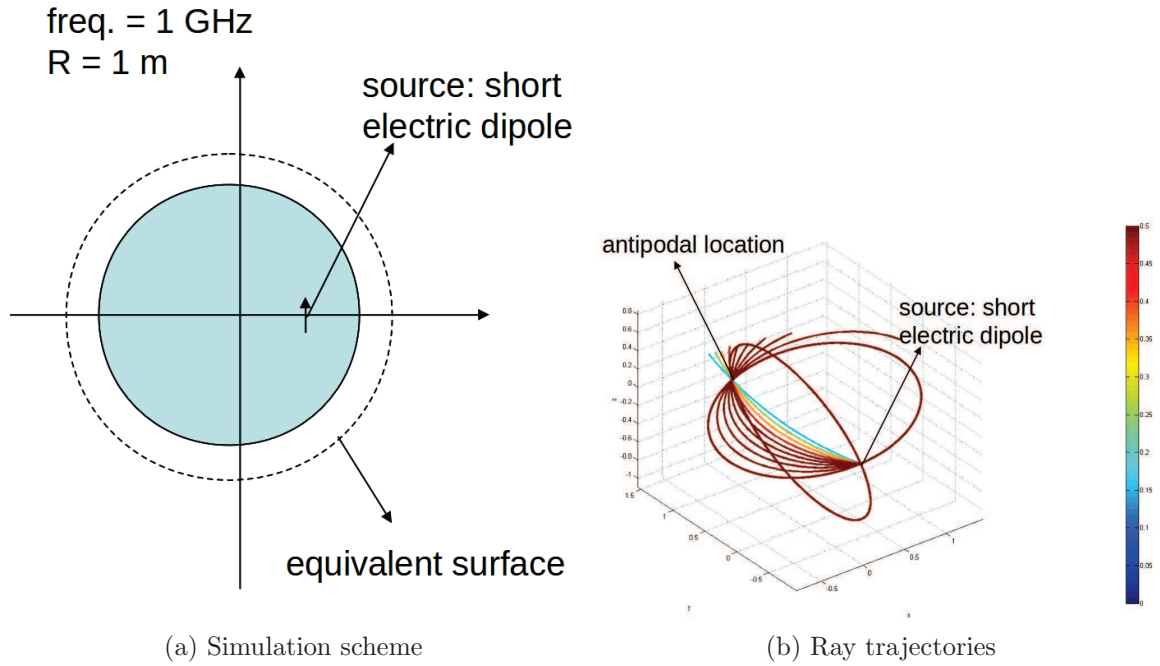
(b) Ray trajectories

Figure 5.2: Maxwell fish eye validation.
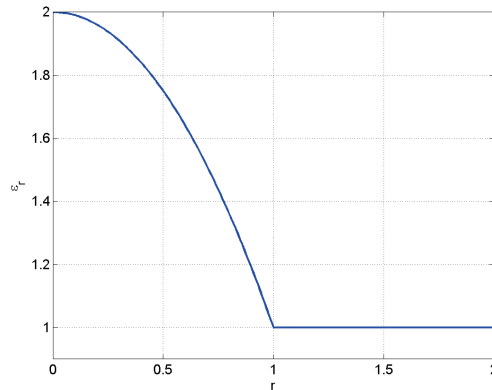
Figure 5.3: ϵ_r profile for Lunenberg lens.

5.2   Scattered Field

In this section the total far field produced by a wave - dielectric system is validated. The previous section studied the rays trajectories, here the complete tool is validated. Validating the scattered field, two stages of the tool may be considered correct:

1. RT Stage: corresponding to the trajectory of the rays and the field associated
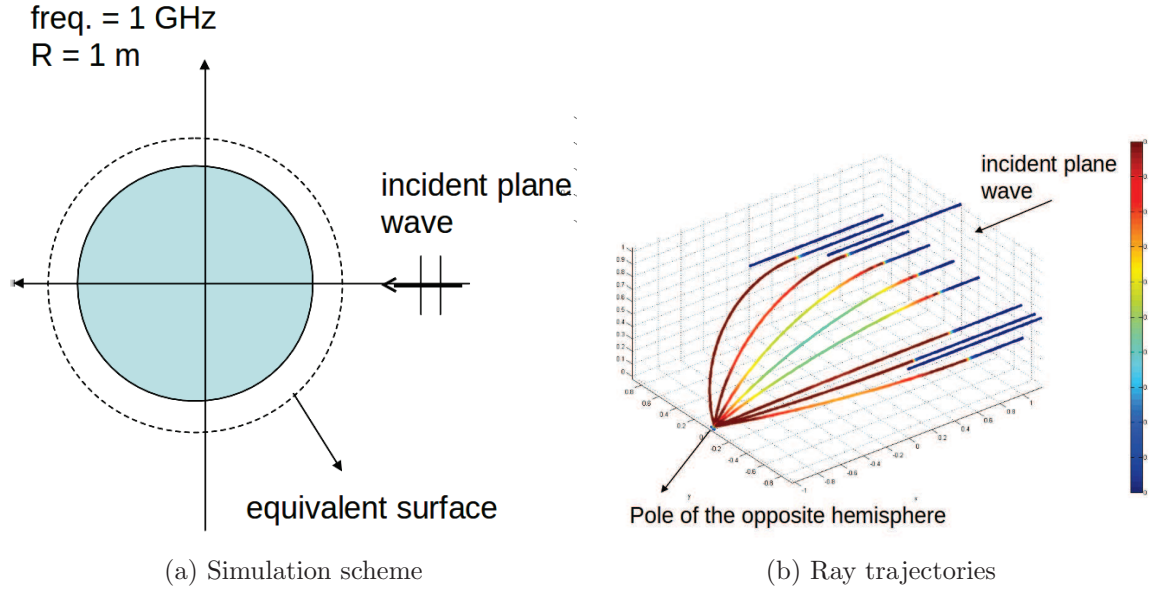
(a) Simulation scheme

(b) Ray trajectories

Figure 5.4: Lunenberg lens validation.

to each one.

2. Radiated Field from equivalent surface to any far field point.

Inhomogeneous dielectric sphere plane wave scattering

To observe if the tool gives a reliable result is necessary to compare it with other method. The final result in this tool is the scattered field that will be also calculated with an analytical solution. The medium used in both cases is a spherical symmetric medium with dielectric constant given by:

$$\epsilon_r = \frac{1 + \epsilon_0}{2}\left(1 + \frac{1 - \epsilon_0}{1 + \epsilon_0}\cos(\pi\frac{r}{R})\right) \tag{5.3}$$

The dielectric profile is reported in figure 5.5.

The analytical solution is obtained from a spherical symmetric medium with step-wise dielectric constants (value sampled from the inhomogeneous sphere).

The incident field is a planewave with frequency 2 GHZ, and the dielectric sphere has radius equal 10 λ.

The pattern is showed in figure 5.6. The behaviour is very close to the reference case that is obtained analytically.
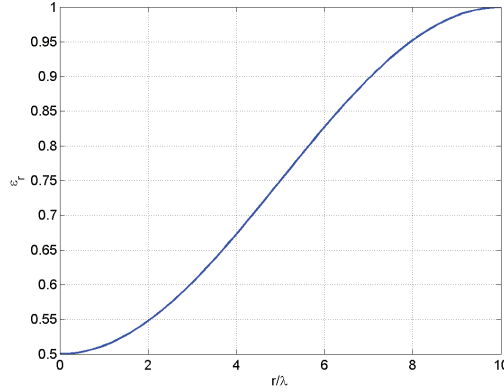
Figure 5.5: Inhomogenous Sphere profile $R = 10\lambda$ and $\epsilon_0 = 3$

5.3   3D spline interpolation

The interpolation of dielectric data is necessary to have a complete model of the plasma in each point where the rays could arrive. The interpolation must be smooth and represent correctly the inhomogenous dielectric body. In this section we check the ray trajectories, equivalent current and scattered field of the interpolated medium compared with a analytical set of points. The interpolated model is builded from a cloud of points, the analytical data can be calculated in each point using the equations.

To check the 3D spline interpolation the inhomogeneous dielectric sphere of section 5.2 is used.

Ray trajectories

In this case a dipole located in (0.0, 0.5, 0.0) and oriented in $+z$ is the source (inside the dielectric sphere). The frequency of work is 2 GHZ and the radius of sphere is 1.5 m (10 λ). In figure 5.7 the set of rays traveling inside an analytical description of the body are compared with the rays in the interpolated model.

Equivalent Sphere

The dipole source is located in (0.0, 1.0, 1.0), oriented in $+z$. In this case the dimension and profile of the inhomogeneous dielectric sphere are as in the previous one and the frequency is 2 GHZ. Figure 5.8 shows the equivalent currents for the
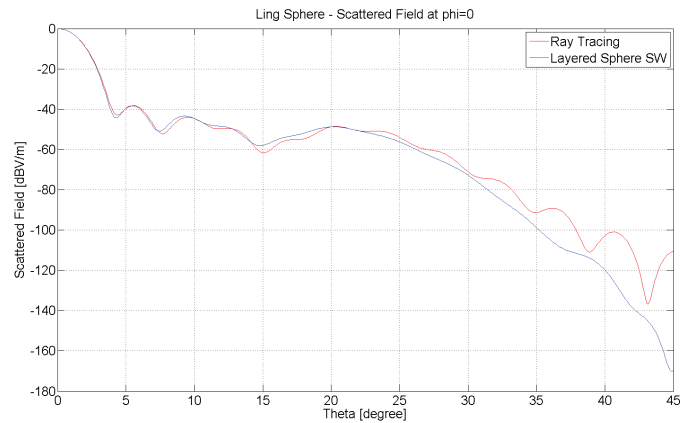
(a) θ from 0 to 45
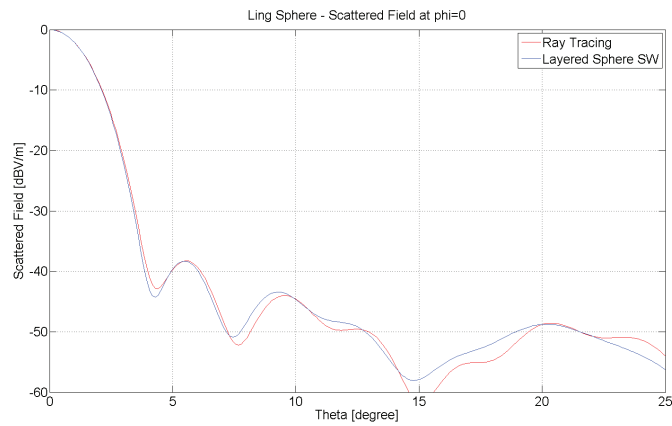
(b) θ from 0 to 25

Figure 5.6: Plane Wave incidence on a inhomogenous dielectric sphere

analytical and the interpolated dielectric body model.

Scattered Field

The last validation of the interpolated dielectric model is related to the scattered field. Figure 5.9 shows the magnitude and phase of the scattered field using analytical and interpolated dielectric body data. The source is a dipole located in (0.0, 1.0, 1.0) and oriented in $+z$. The work frequency is 2 GHz and the sphere radius is 1.5 m (2 λ). The cuts in the figure are the XZ planes of the radiated field.

31

Analytic plasma / Rays

Ray Tracing with 3D interpolation

(a) Analytic dielectric profile

(b) Interpolated dielectric profile

Figure 5.7: Ray trajectory in interpolated dielectric body

Analytic Plasma Result
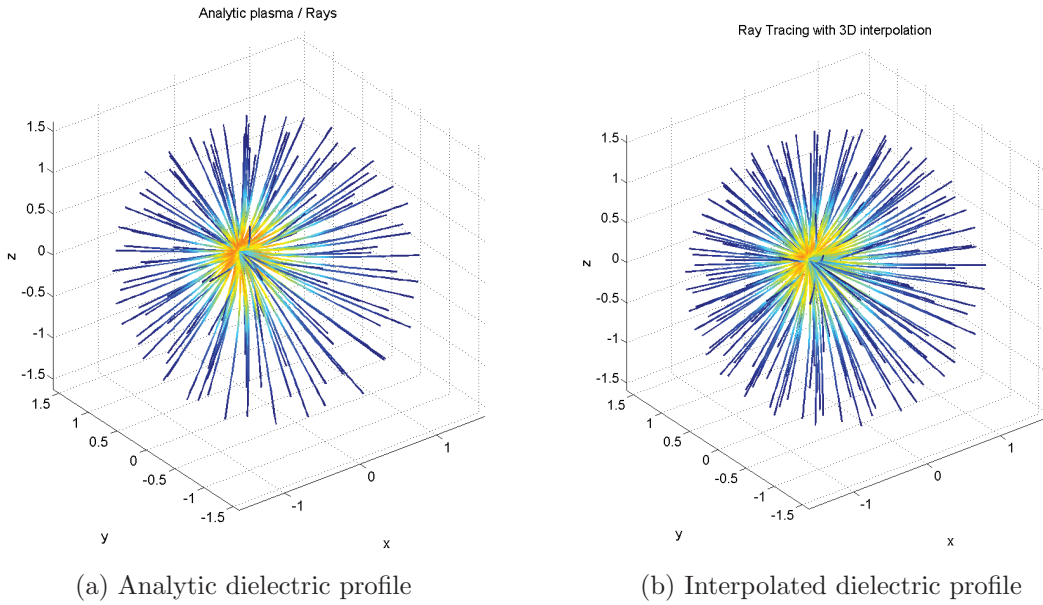
Equivalent Current with 3D interpolation

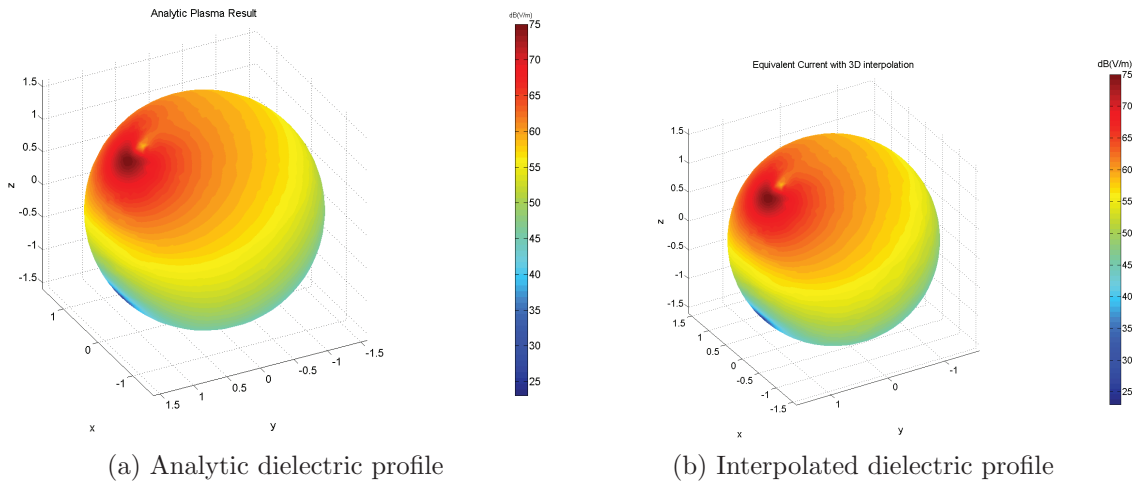(a) Analytic dielectric profile

(b) Interpolated dielectric profile

Figure 5.8: Equivalent current for interpolated dielectric body

5.4 Presence of the vehicle

The tool considers also the presence of an metallic object, reflecting the rays. The ray reflection must also correct the related field with the Perfect Electric Conductor conditions.

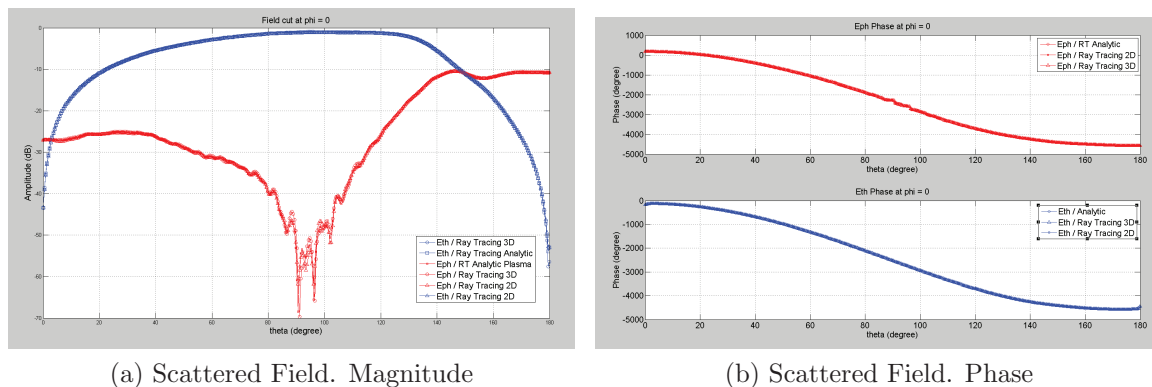(a) Scattered Field. Magnitude   (b) Scattered Field. Phase

Figure 5.9: Analytical vs. Interpolated models.

Scattered Field

The first system to evaluate is a dipole-disk scheme. Ray-tracing approach is compared with the complete MoM solution. The scattered field is the observable characteristic. The figure 5.10 shows how the system has been positioned. The disk has a diameter of 10 λ, the dipole is oriented in $\hat{x}$ and the distance from the disk is 2.25 λ. The antenna is also misaligned respect to the disk axis, to avoid symmetry effects.

The structure has been simulated in free space to compare the results with MoM simulations.

The electric scattered field magnitude is showed in figure 5.11a that shows a good agreement with the reference simulations . The phase of the electric field is reported in figure 5.11b.

Ray trajectories and phase

Even if the field scattered by an object gives us a good idea of the reliability of the results, we wanted to observe a pair of properties that must be respected in a electromagnetic field interacting with an metallic object. A parabolic reflector is a particular and useful case of test. There are two properties that is possible to verificate visually. First, a spherical wave with center (source) in the paraboloid focus becomes a plane wave, in other words all the rays from the focus are reflected in a parallel array. Second, a plane wave has planar wavefronts (planes with same phase) because rays travel the same distance. So, we can see that all rays after reflection on a paraboloid will be parallels and the phase on a plane orthogonal to the parabola axis will be constant. The testing system is reported on figure 5.12. The diameter is $D = 4\lambda$ and the ratio f/D is equal to 0.25. The frequency is 600 MHz and the focus distance is λ.

33
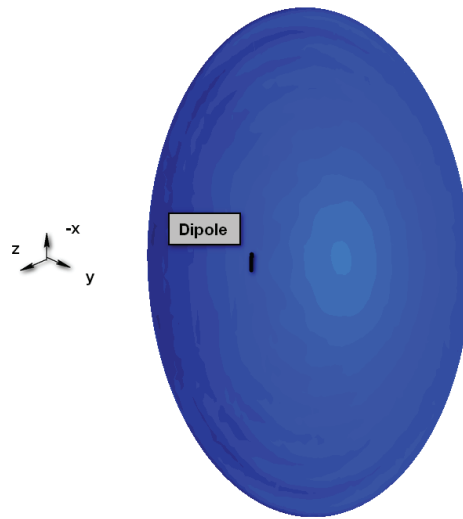
Figure 5.10: PEC plane disk

In the figure 5.13 the rays related to the reflected plane wave are showed. Figure 5.14 is a graphical representation of a planar wavefront, the phase is constant in any plane orthogonal to the paraboloid axis.
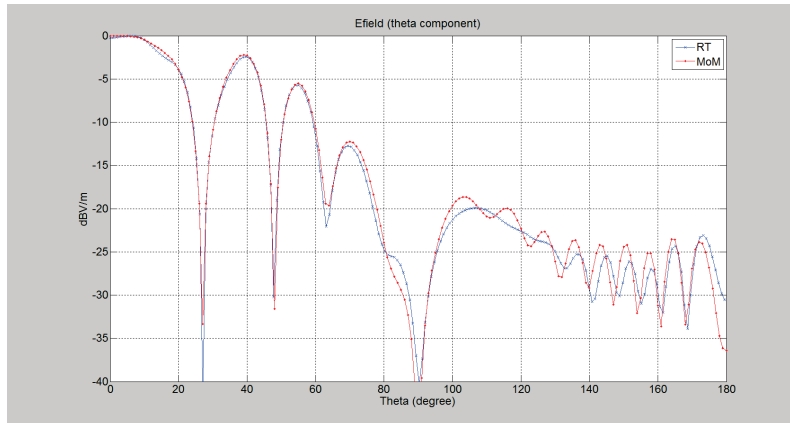
(a) Dipole and disk. Scattered Field. Magnitude
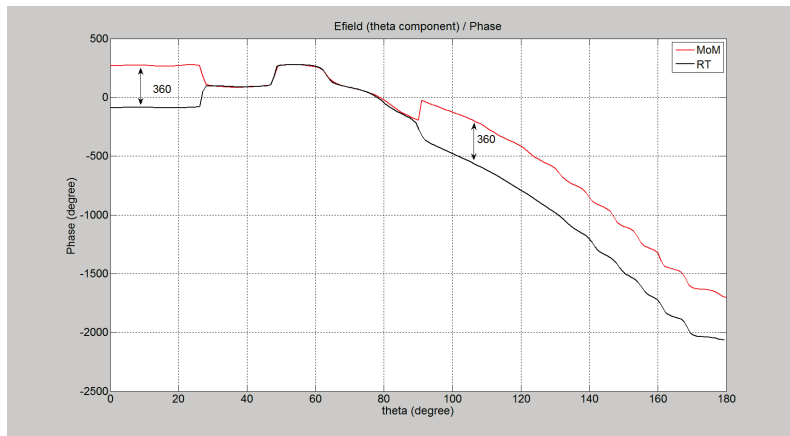
(b) Dipole and disk. Scattered Field. Phase

Figure 5.11: Dipole-disk system
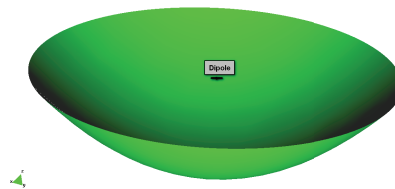
Figure 5.12: Dipole and paraboloid

35
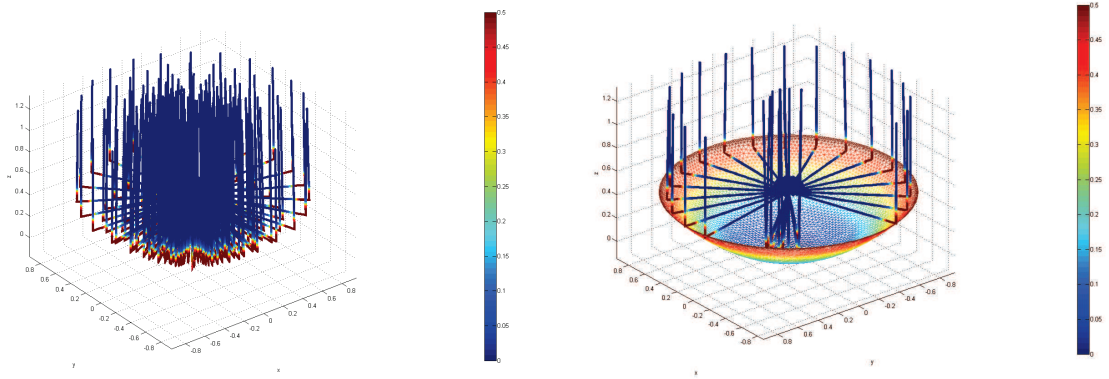
(a) Ray trajectories

(b) Ray trajectories and object

Figure 5.13: Reflected rays on a parabolic surface
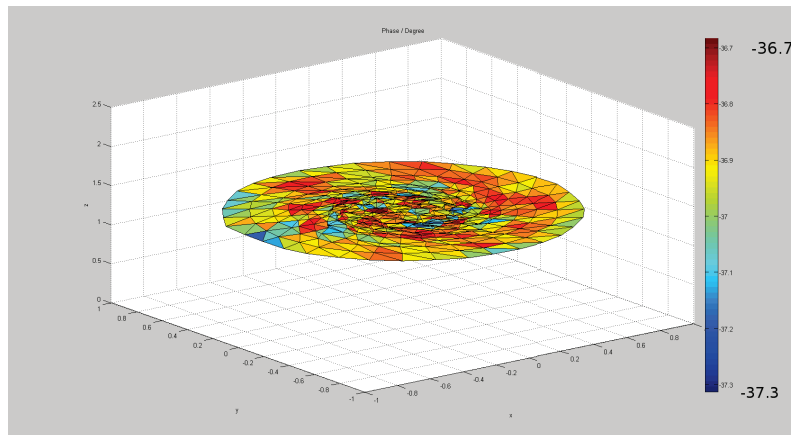
Figure 5.14: Phase after reflection on paraboloid

Chapter 6

Numerical results

This chapter is a collection of some results obtained using the EM solver in a realistic case. Simulated plasma data (CFD) is used as input, and all the stages of the tool are involved in the process.

6.1   IXV (S-band)

The results presented here are obtained for the ESA (European Space Agency) Intermediate eXperimental Vehicle (IXV) that is under projectation. Figure 6.1a depicts the position of the antenna on the vehicle surface and fig. 6.1b the plasma cloud around it.

(a) frequency = 2.6 GHz (S band)   (b) IXV Mach 25 log plasma freq.
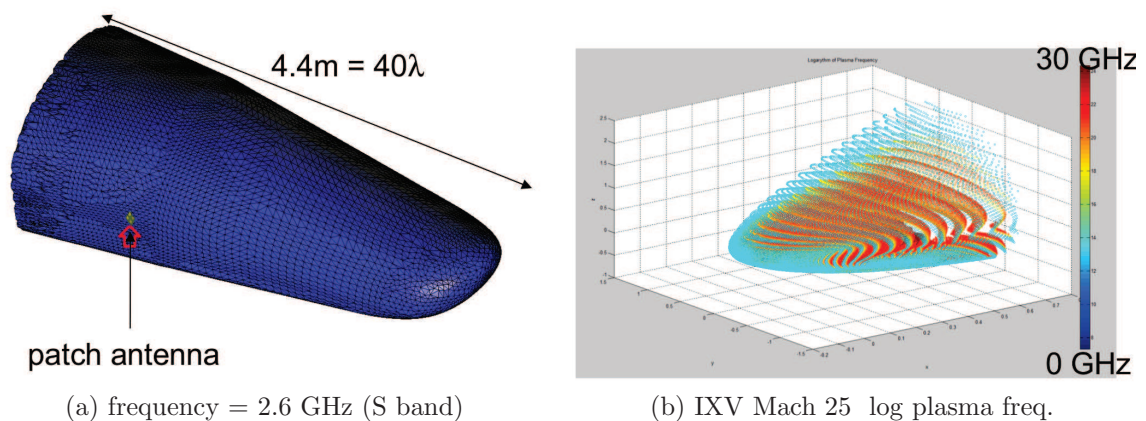
Figure 6.1: IXV and plasma

Pattern cuts

The first results shown are some pattern cuts in the main planes (XY, YZ, XZ) in figures 6.2, 6.3 and 6.4. The comparison against the free space pattern gives a good impression about the plasma effect on the propagation: The pattern is focused in some areas, and is almost null in the region where the plasma cloud is denser and hotter. Normally the rays that does not exits on the dense plasma region are redirected to regions when the transition is slower, and reach the equivalent surface in that zones.
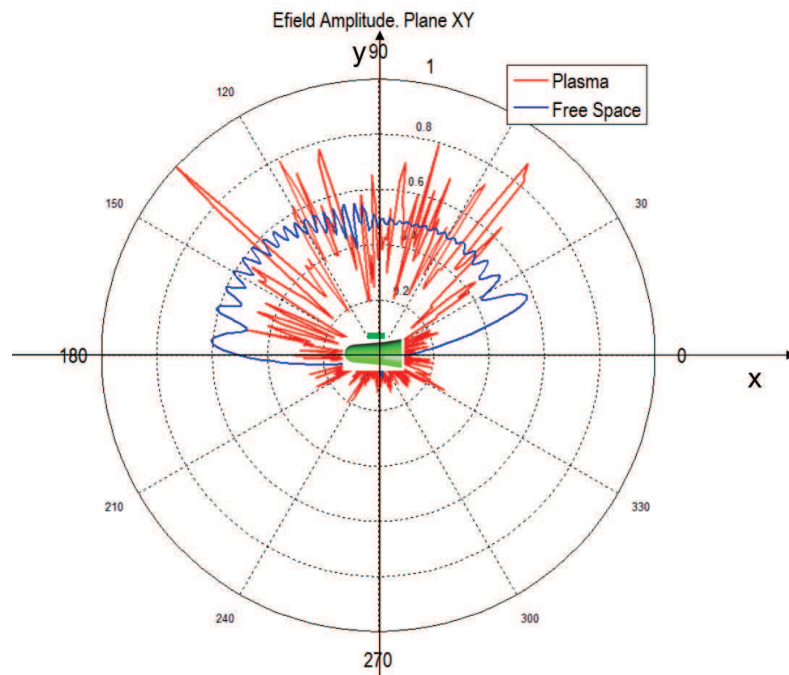
Figure 6.2: IXV simulation, XY cut.

Spherical pattern

The results in this section permits to see how the plasma affects the pattern while becoming denser. Using the same antenna configuration and pattern used in the previous section, a spherical pattern is calculated for each plasma "snapshot" available. The spherical pattern is depicted on a plane projection and the coordinates system is the antenna reference frame.

The information of the spaceship trajectory and speed is added. Is possible to see in figures 6.5, 6.6, 6.7 and 6.8 how the pattern is more affected as the spaceship

38
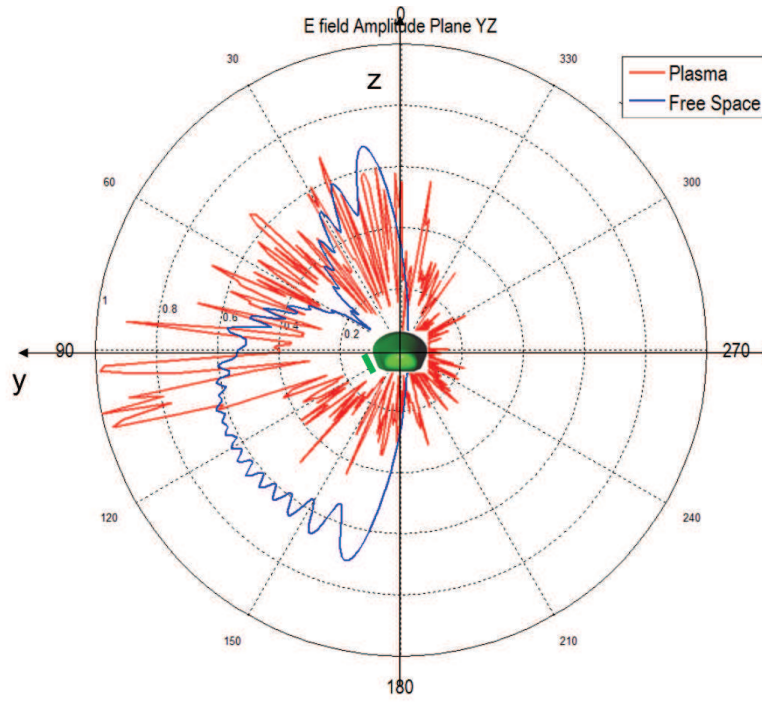
Figure 6.3: IXV simulation, YZ cut.
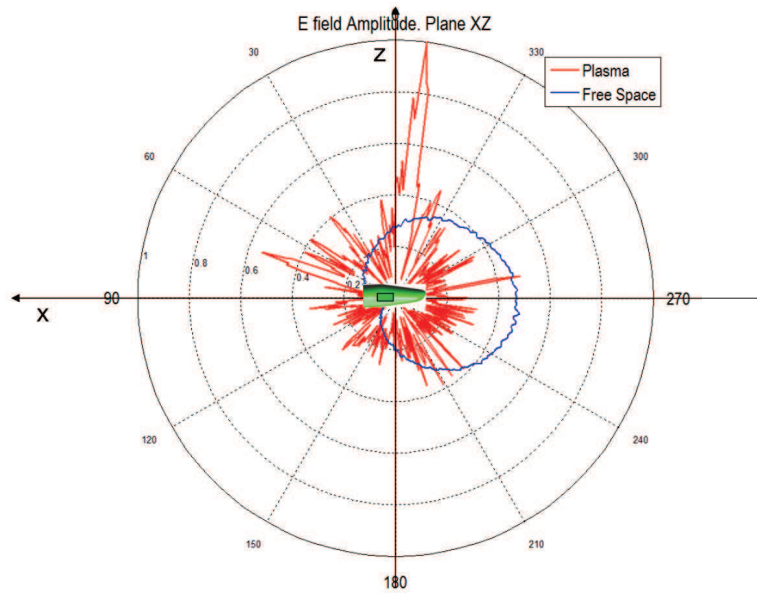
Figure 6.4: IXV simulation, XZ cut.

speed is higher and the plasma shield stronger. Figure 6.9 shows the free-space

39

antenna pattern.

(a) Spherical pattern

(b) Position and speed

Figure 6.5: IXV. Mach 25

(a) Spherical pattern

(b) Position and speed
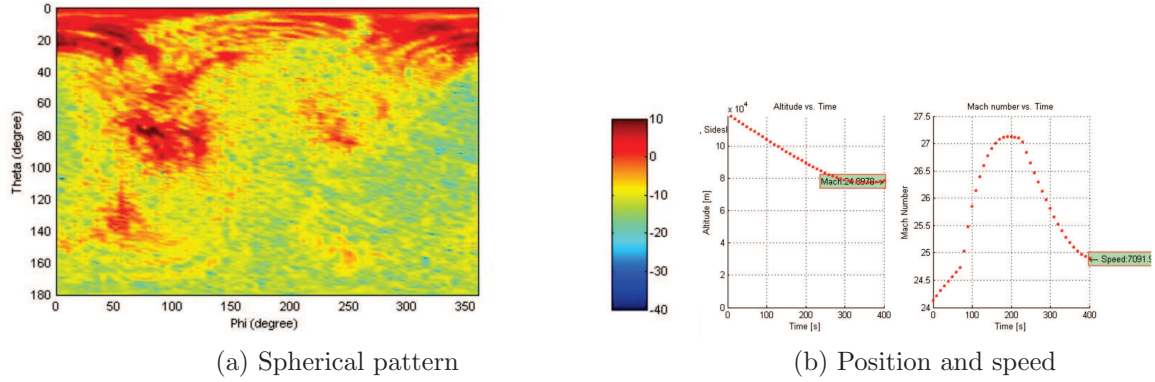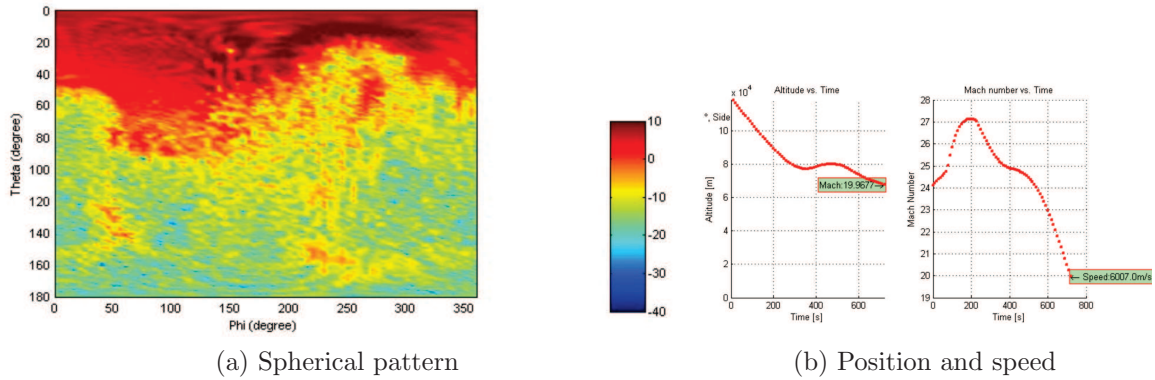
Figure 6.6: IXV. Mach 20

6.2 ARD

The Advanced Reentry Demonstrator (ARD) was a suborbital reentry test flown on the third Ariane 5 flight in 1998. For the ARD vehicle are available two plasma "snapshots": Mach 20 and Mach 24.

One of the main goals in developing the plasma simulation tool was the option to check how different antenna position and communication characteristics affect the propagation in the plasma-vehicle system. In this section some simulations are performed on the ARD spaceship, changing antenna position or link frequency.

In table 6.1 are collected 4 options of antenna position, and figure 6.10 shows the reference system. The $+z$ is on top of the vehicle, where a denser plasma is present

(a) Spherical pattern

(b) Position and speed

Figure 6.7: IXV. Mach 17

(a) Spherical pattern

(b) Position and speed
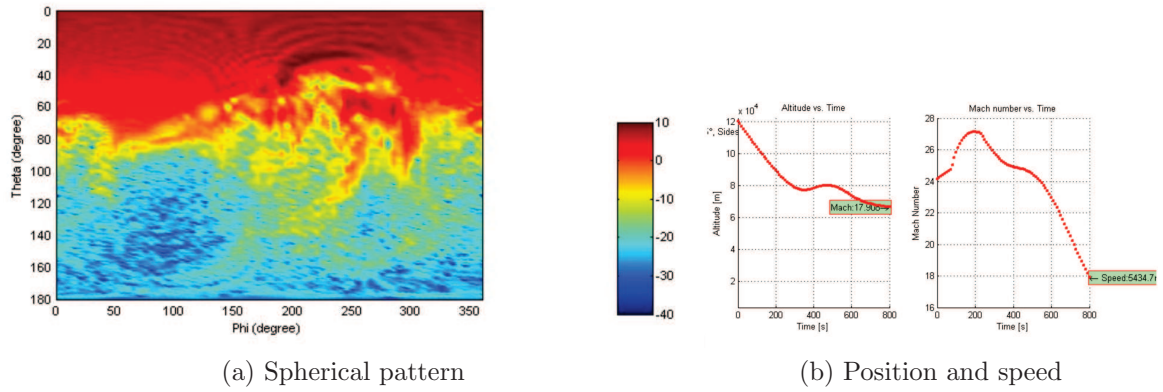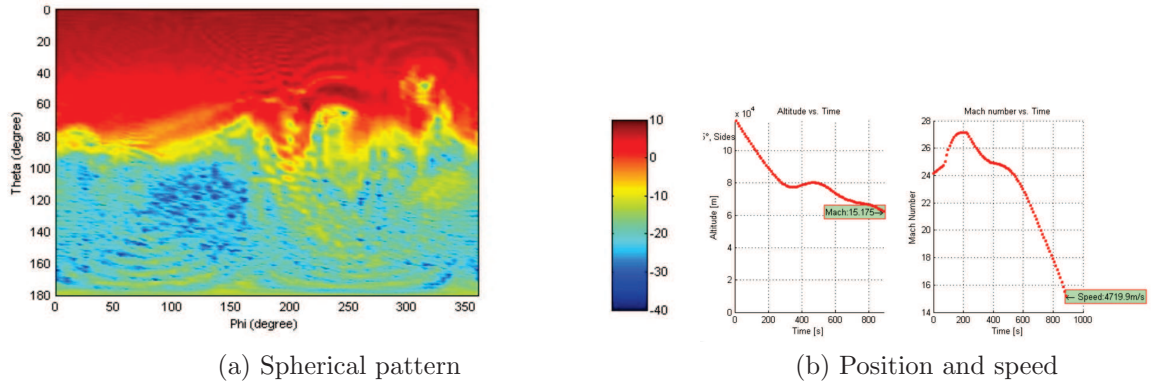
Figure 6.8: IXV. Mach 15

(a) Spherical pattern
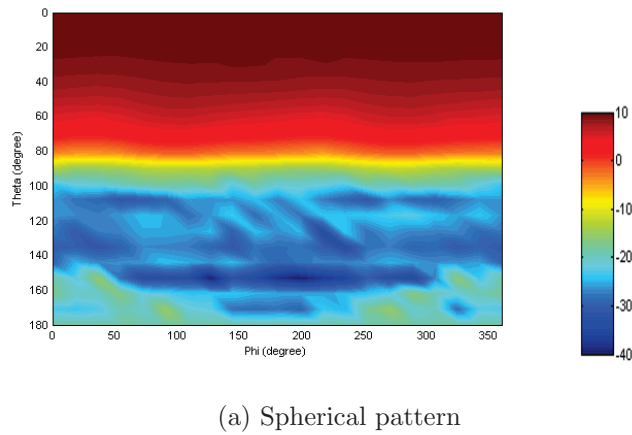
Figure 6.9: IXV. Free Space

41

(fig. 6.10b), while the bottom antenna has space to propagate.

Figure 6.10b shows the plasma frequency. The blockage of the communication channel depends on the relation between link frequency and plasma frequency (cut-off). The first case of study is in S-band (2.26 GHz). The $+z$ antenna is completely blocked by the plasma in the mach 24 case, the plasma frequencies are above the link frequency, giving a cut-off layer surrounding the antenna and producing a complete blackout as in fig. 6.11b. In the mach 20 situation, there is antenna information exiting the plasma cup.

If antenna is located on $-z$ position there is communication in both the plasma cases, the pattern is affected but the source is not completed hidden by the plasma (fig. 6.12). A similar situation is seen in $+y$ (or $-y$ by plasma symmetry) but the pattern distortion is smaller because the main plasma wake is in the direction of movement, on top and botton the vehicle.

Installation vehicle side	x coord.	y coord.	z coord.
+Y	1.081	0.998	0.000
-Y	1.081	-0.998	0.000
+Z	1.081	0.005	0.998
-Z	1.081	0.005	-0.998

Table 6.1: ARD antenna position

At higher frequencies, the plasma attenuation affect less the radiation pattern characteristics. Figures 6.14 and 6.15 are the results for the simulation in C-band (7.19 GHz) in the same $+z$ and $-z$ positions presented before. The total blackout in mach 24 is no produced at this link frequency, and antenna pattern is less modified than in the previous case for the other antenna and vehicle speed configurations.

(a) Body reference system   (b) $+/-z$ antennae.   (c) Vehicle and $+y$ antenna.
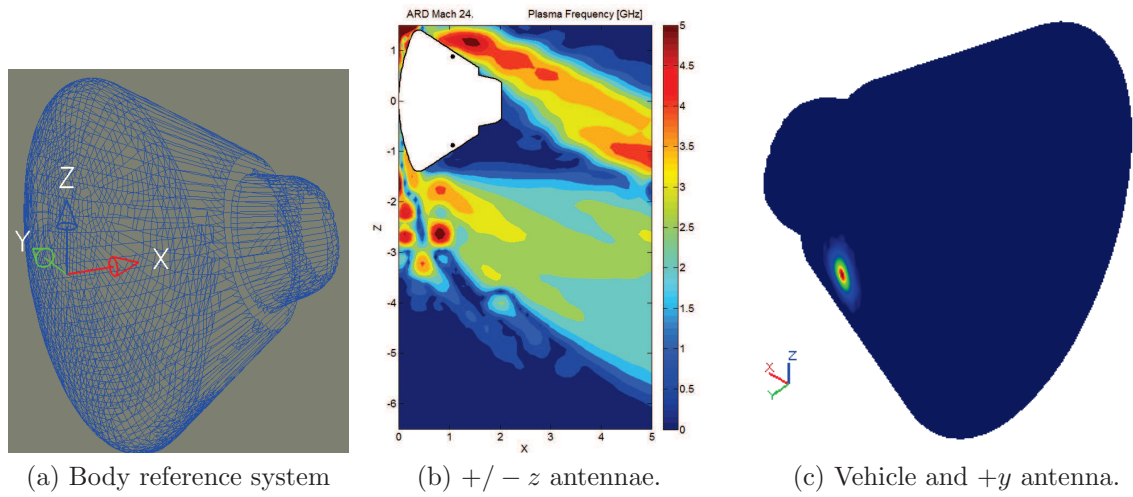
Figure 6.10: ARD-plasma reference system.

(a) Mach 20   (b) Mach 24. Black-out
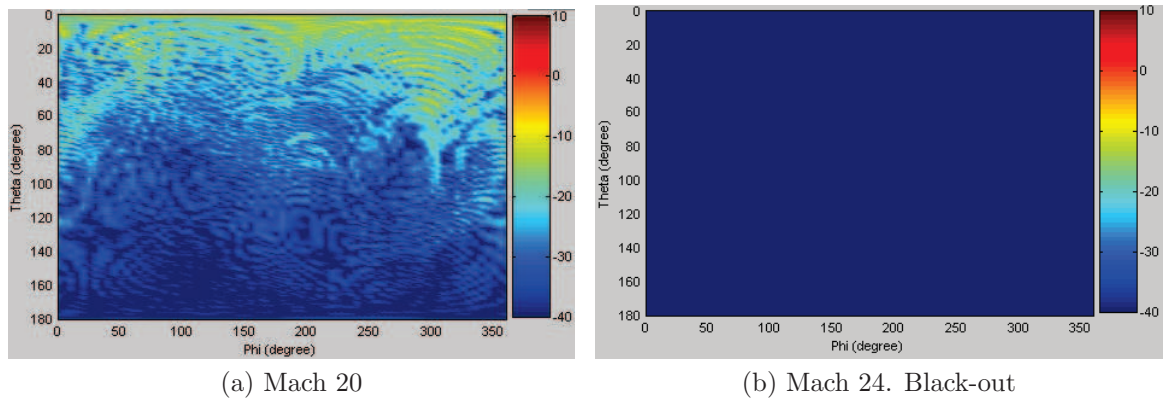
Figure 6.11: ARD. Antenna on $+z$. S-band
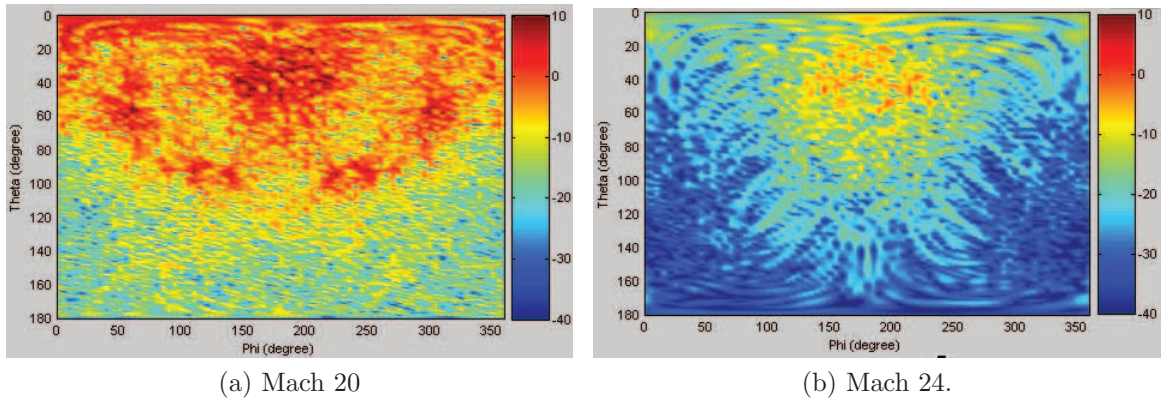
(a) Mach 20

(b) Mach 24.

Figure 6.12: ARD. Antenna on $-z$. S-band
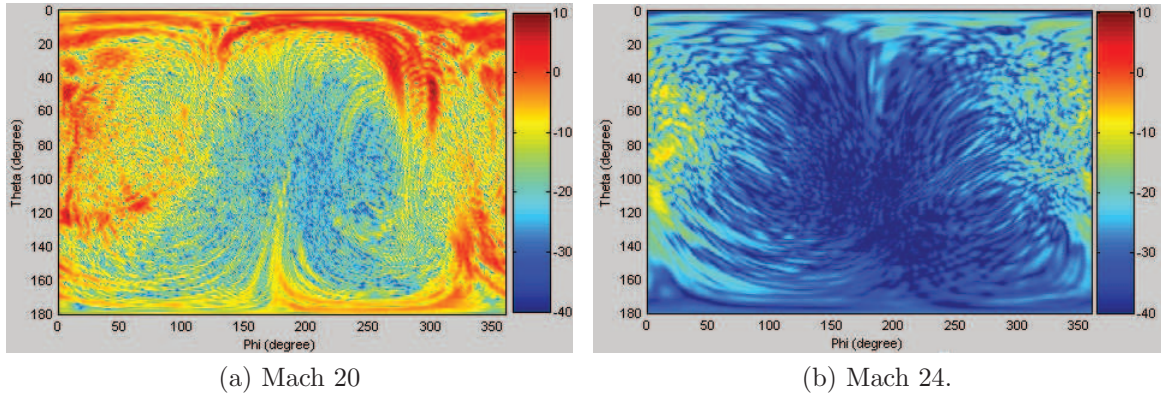
(a) Mach 20

(b) Mach 24.

Figure 6.13: ARD. Antenna on $+y$. S-band
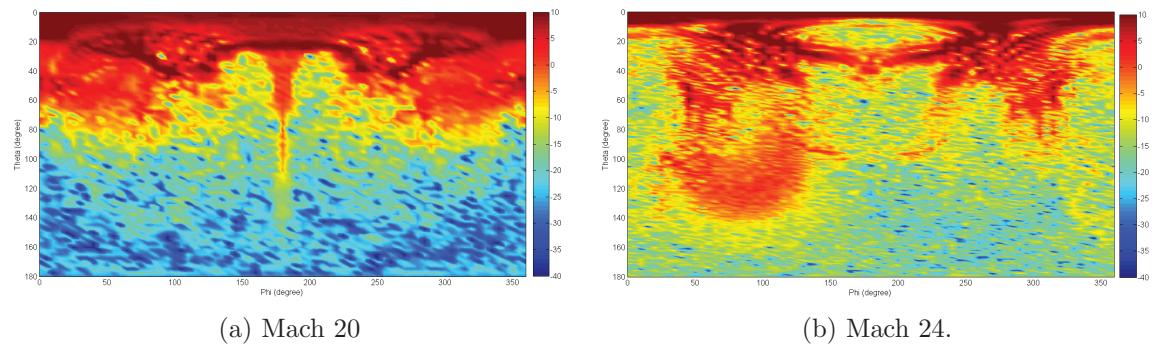
(a) Mach 20

(b) Mach 24.

Figure 6.14: ARD. Antenna on $+z$. C-band

44
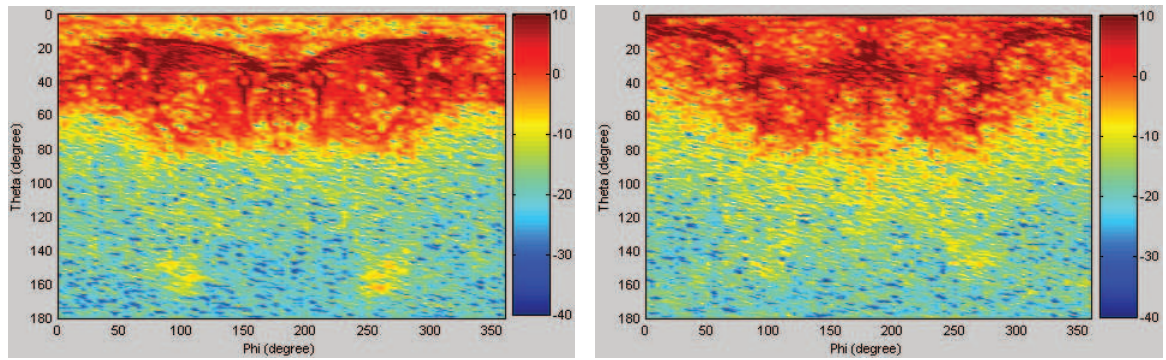
(a) Mach 20

(b) Mach 24.

Figure 6.15: ARD. Antenna on $-z$. C-band

45

Chapter 7

Conclusions

The main result of the present work is the Propagation In Plasma tool itself. The modeling of the plasma cloud as an inhomogeneus dielectric body, the eikonal equation approximation (ray tracing) and the equivalence principle permit to predict, all together, the pattern distortion of an antenna located on a re-entry vehicle.

The plasma dielectric model is obtained from the Computed Fluid Dynamics (CFD) simulations. This simulations give a group of data related to the heating and ionization of the air around the spaceship. The ionization is the main information related to the plasma dielectric characteristic. To obtain a "any-point" dielectric model, a 3D interpolation is used. The spline interpolation is choosen because its smoothness and low-degree features.

The approximation of ray tracing inside the plasma (ray curvature depends on dielectric characteristics variation)is complemented with the exact radiation calculation from the equivalent surface. The equivalent surface encloses the plasma-vehicle system and is obtained after the ray tracing process.

But not only the Propagation In Plasma tool is a result of this research. Can be considered also as results some conclusions extracted from the simulations done in the IXV and ARD cases.

The first is related to the antenna position. Is true that a high plasma shield blocks the signals travelling away the spaceship, but is also true that the position of the antenna source is determinant for this blockage. As seen in chapter 6 the blackout is avoided if the antenna is located in a different place.

At higher frequencies, the plasma attenuation affect less the radiation pattern characteristics. It could be useful in the projection of the channel stage. Using

simulations of trajectory and plasma is possible to study how the different channel options are affected in each situation.

Remains the case of the pattern distortion (power re-distribution) that can produce a low field condition in a particular direction when plasma is present, against a high field in the free-space case. The presence of plasma focuses the transmitted power on narrow regions decreasing the likelihood of setting up a reliable and long-lasting connection. The simulation tool is useful to determine how the pattern is distorted and to know how the channel characteristics are affected by this. Due to cut-off rays some reduction on the total radiated power is also present.

The Propagation in Plasma tool gives the flexibility needed to project any antenna position, plasma configuration, frequency link, vehicle interaction and wanted direction combitation to characterize the communication channel.

Bibliography

[1] S.M. Rao, D. Wilton and A.W. Glisson *Electromagnetic scattering by surfaces of arbitrary shape.* IEEE Transactions on Antennas and Propagation, vol 30, 1982.

[2] *Study of the radiation of the ARD patch antenna trough plasma during re-entry.* Politecnico di Torino, Torino, IT, ESA Contract, december 2001.

[3] Vecchi, G., Sabbadini, M., Maggiora, R. and Siciliano, A. *Modelling of antenna radiation pattern of a re-entry vehicle in presence of plasma.* Antennas and Propagation Society International Symposium, 2004. IEEE, june 2004.

[4] Kim, H and Ling, H. *Electromagnetic Scattering from an Inhomogeneous Object by Ray Tracing.* IEEE Transactions on Antennas and Propagation, vol. 40, no. 5, may 1992.

[5] Born, M. and Wolf, E. *Principles of optics.* Pergamon Press, Oxford, UK, 1980.

Part II

Automatic h-refinement

Chapter 8

Introduction

The Surface Integral Equation is one of the most used methods in the simulation of electromagnetic problems. The method used a discretized description of the surface on which a number of basis functions are defined. These basis functions approximate the current present on the surface due to an excitation. Each basis function is related to a discretized patch in the surface, so the mesh size determines the number of basis functions used to describe the current. It makes mesh quality and resolution be one of the key issues in the solution of this kind of problems. A fine mesh is required to obtain an accurate current description on the surface.

In the case of multi-scale structures, the test-object has regions with high details that require a fine mesh, together with flat surfaces where the current can be properly described with a coarser mesh. In figure 8.1 an example of multi-scale structure is shown. Usually the detailed regions or the sharp edges require a finer mesh not only to a correct description of the geometry, but also because in this regions the variation of the current is higher and more basis functions are needed.

A standard meshing algorithm generates a mesh only to describe the geometry, has not account of the electromagnetic requirements. A sharp edge can be described geometrically with few mess elements, but will require much more for a correct description of the current. Usually a conservative approach is followed: To have a fine mesh in all the surface, leading to a total number of unknowns can be much higher than the minimum required for a specific accuracy.

A high number of unknows implies, consequently, that the computational cost of the solution will be superior to the actually needed, in terms of memory and processing time. The current in some regions will use more basis functions that the actually needed. These extra basis functions could be used in regions where accuracy is more difficult to achieve.

(a) Details   (b) Object   (c) Flat Regions
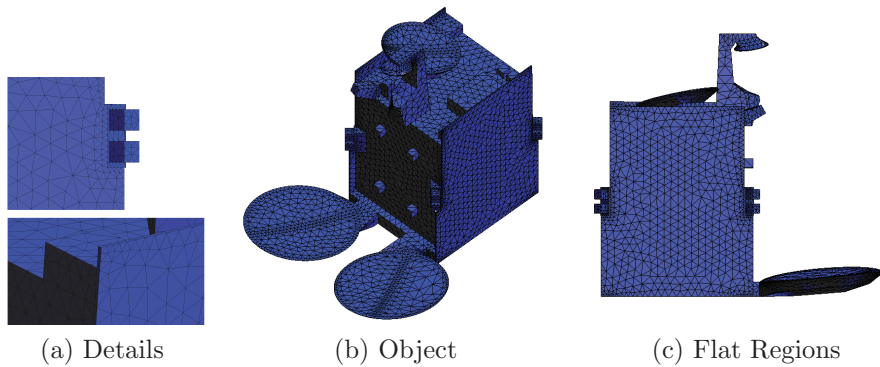
Figure 8.1: Multi-scale structure
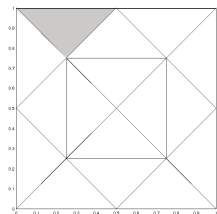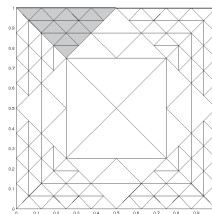
(a) Initial mesh (Conformal)   (b) Final mesh (Non-conformal)

Figure 8.2: Localized refinement

A standard mesh algorithm and the lack of an a-priori knowledge of the error on the unknown current, lead to an uniform and non-optimal mesh. The requirement of discretization conformity imposed by the usual surface integral equation formulations is other obstacle to an optimal mesh.

The goal of this work is to develop an automatic tool that identifies the regions to be refined in a initial coarse mesh (defined only by geometry). In the identified regions a local refinement is applied, it generates a non-conformal mesh as can be seen in figure 8.2. Hence the resulting integral equation is solved through a Discontinuous Galerkin scheme, able to handle this kind of meshes.

51

Chapter 9

Surface Integral Equation and Discontinuous Galerkin

For the electromagnetic analysis, normally the first-order continuity of the basis functions used in the numerical solution (either normal or tangential components of the vector functions) is preserved. In order to accomplish this, the surface-patch models must be conforming. Conforming cells have their edges and corners aligned so they yield a continous surface (although not necessarily a smooth one) as in fig. 8.2a. Nonconforming models might have gaps between adjacent cells, and be unsuitable for providing a continous expansion.

A method that does not require this continuity in the cells could do mmesh definition ore flexible, and can also permit the h-refinement that is the goal in this work.

In this chapter the Surface Integral Equation is extended to a non-conforming method. The usual formulation of the Surface Integral Equation is based on Continous Galerkin (CG), that is conforming. The Discontinous Galerkin (DG) method overlays on a trial function space that is piecewise discontinuous, that is more general and gives flexibility in the definition of the domain.

In this particular case the extension permits to use non-conforming triangular meshes instead of the usual conformal triangular meshes.

9.1 Formulation

The considerations presented in this chapter are focused in the Surface Integral Equation case for a PEC case but the method is, indeed, general. The object surface is denoted by S, and it is discretized by a mesh of triangular cells.

The Standard Integral Equation method is the Galerkin method applied to the radiation equations. Galerkin methods are a class of methods for converting a continuous operator problem (such as a differential or integral equation) to a discrete problem. In principle, it is the equivalent of applying the method of variation of parameters to a function space, by converting the equation to a weak formulation. Typically one then applies some constraints on the function space to characterize the space with a finite set of basis functions.

In the case of the Surface Integral Equation, the operators are the electric and magnetic field operators (L and K) that give the electric and magnetic radiated field from a current. The basis functions are divergence free and continious on the discretized geometric space (surface), usually Rao Wilton Glisson basis functions. The discretization of the surface is obtained by triangular patches.

The current on the surface $\mathbf{J}$ is approximated by

$$\mathbf{J} = \sum_{i=1}^{N} I_i \mathbf{f_i} \tag{9.1}$$

where I_i is each one of the coefficientes to be find and $\mathbf{f_i}$ the relative basis function.

The standard Surface Integral Equation is defined, considering the said before, as:

$$\underbrace{a_1 \langle \mathbf{v}, \mathbf{R}^{(E)} \rangle_S}_{\text{Standard EFIE term}} + \underbrace{a_2 \langle \mathbf{v}, \mathbf{R}^{(M)} \rangle_S}_{\text{Standard MFIE term}} \tag{9.2}$$

where $\mathbf{R}^{(E)}$ and $\mathbf{R}^{(M)}$ are the electric and magnetic residuals, and $\mathbf{v}$ are the testing functions (in Galerkin approach the testing functions $\mathbf{v}$ are the same basis function $\mathbf{f}$. The residuals are defined as

$$\mathbf{R}^{(E)} = L\{\mathbf{J}\} - \hat{\mathbf{n}} \times \mathbf{E^{inc}} \tag{9.3}$$

and

$$\mathbf{R}^{(M)} = (\eta_0(\mathbf{n} \times \mathbf{H}^{inc}) + \frac{1}{2}\mathbf{J} + \mathbf{n} \times K\{\mathbf{J}\}) \tag{9.4}$$

where L and K are the electric and magnetic field operators.

The residues are forced to zero, setting the linear system that, solved, gives the coefficients of the current.

The usual Surface integral Equation is defined for conforming meshes. A general case would contain a non-conformin discretization. It implies a different formulation, that has into account the discontinuity od the basis function. Figure 9.1 shows two adjacent triangles in a non-conformal mesh, the notation is used in the following sections where new formulation is defined.
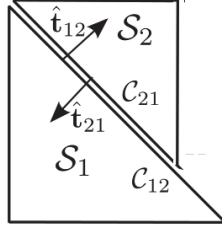
Figure 9.1: Adjacent Elements in generic (non-conformal) mesh.

In the case of non-conformal mesh the edge based basis functions (as standard RWG [1]) cannot be defined, cell-based basis functions are used instead. As consequence, the continuity of normal component of the current is not enforced across the countour boundaries, and line charges may accumulate along.

New conditions are added to penalize the accumulation of line charges on the countour boundaries. In the standard Surface Integral Equation it was forced in the definition of the basis functions. In the Discontinous Galerkin method discontinous basis functions are used, and the continuity is forced weakly.

Interior Penalty Formulation

The first condition is related to the continuity of the current across the boundary. A trasmission continuity is forced on the countour C_{mn} and C_{nm}, between triangles S_1 and S_1 (figure 9.1). The current going from one triangle to other is equal (in the common edge) as

$$\mathbf{t}_{mn} \cdot \mathbf{j}_m(\mathbf{r}) = -\mathbf{t}_{nm} \cdot \mathbf{j}_n(\mathbf{r}) \tag{9.5}$$

A new error residual is defined from this continuity condition

$$R^A_{C_{mn}} = \sum_{C_{mn} \in C} \frac{1}{jk_0} (\mathbf{t}_{mn} \cdot \mathbf{j}_m + \mathbf{t}_{nm} \cdot \mathbf{j}_n)(\mathbf{r}) \tag{9.6}$$

and a Boundary Penalty term is include as a new term in the formulation to penalize the accumulation of charge, testing it with the normal component of the functions on the edge C_{mn}

$$\langle \mathbf{t}_m \cdot \mathbf{v}_m, R^A_{C_{mn}} \rangle \tag{9.7}$$

A second condition to be added might be the continuity of the current as before, but through an integral operator

$$L_{C_{mn}}(\mathbf{t}_{mn} \cdot \mathbf{j}_m(\mathbf{r}) + \mathbf{t}_{nm} \cdot \mathbf{j}_n(\mathbf{r})) \tag{9.8}$$

the integral operator $L_{C_{mn}}$ is the standard Electric Field Integral Operator but defined only on the edge where the continuity is forced. This integral operator is

$$L_{C_{mn}}(\mathbf{f}) = \frac{1}{jk_0} \int_{C_{mn}} G(\mathbf{r}', \mathbf{r}) \cdot \mathbf{f}(\mathbf{r}') d\mathbf{r}' \tag{9.9}$$

The error residual due to this new defined condition is

$$R^B_{C_{mn}} = \sum_{C_{mn} \in C} T_{C_{mn}}(\mathbf{t}_{mn} \cdot \mathbf{j}_m(\mathbf{r}) + \mathbf{t}_{nm} \cdot \mathbf{j}_n(\mathbf{r})) \tag{9.10}$$

The residual $R^B_{C_{mn}}$ can be read as the electric potential due to the accumulated charges in the edge, we must ensure that no energy is produced by accumulated charges by

$$\langle \mathbf{t}_m \cdot \mathbf{v}_m, R^B_{C_{mn}} \rangle \tag{9.11}$$

So, the second term penalizes the radiation of accumulated charges, which implies that this charges are equal to zero when the problem is solved.

Summarizing all the residuals, adding to the standard the new penalty terms that had been defined, the new formulation for the Surface Integral Equation (Discontinous Galerkin) is

$$\underbrace{a_1 \langle \mathbf{v}, \mathbf{R}^{(E)} \rangle_S}_{\text{Standard EFIE term}} + \underbrace{a_2 \langle \mathbf{v}, \mathbf{R}^{(M)} \rangle_S}_{\text{Standard MFIE term}}$$

$$+ \underbrace{a_3 \langle \mathbf{t} \cdot \mathbf{v}, \mathbf{R}^{(A)} \rangle_C}_{\text{Interior Penalty term - Continuity}} + \underbrace{a_4 \langle \mathbf{t} \cdot \mathbf{v}, \mathbf{R}^{(B)} \rangle_C}_{\text{Interior Penalty term - Charge Radiation}} = 0 \tag{9.12}$$

The Discontinous Galerkin formulation for Surface integral equation has been presented originally in [2], arriving to the equation 9.12.

The choice of a_1, a_2, a_3 and a_4 can be determined by the considerations of accuracy and/or convenience. The new interior penalty terms are defined only on the boundary edges, where the conditions of continuity are set to avoid the accumulation of charge.

9.2 Fast iterative solver with Surface Integral Equation (DG)

When large structures are involved, the direct solution of the linear system is not feasible, and a fast method is needed.

The Discontinous Galerkin Surface Integral Equation described in the previous section can be extended to any fast method, adding the two new penalty terms presented in equation (9.12), to the terms already implemented in the fast method.

In this particular case the Green's interpolation with fast Fourier transform (GIFFT) is used. The Green's function is mapped onto a regular cartesian grid, and the fast Fourier transform (FFT) is used in the convolution products. As the penalty terms are defined on the contour of the mesh triangles (C), the approach is quite similar to the wire-surface fast solver presented in [3] as extension of the solver in [4].

The choice of coefficientes in eq. (9.12) can eliminate the problematic double contour integral related to edge-edge interaction. Successive simplification leads to a IEDG formulation where the extra terms are the interaction between the divergence of surface functions and the projection of the functions on the edges.

The main idea in the GIFFT is to expand the free-space Green's function in terms of Lagrange polynomials, defined on the regular grid. The system matrix can be factorized as

$$[Z] \approx [Z^P] = \frac{1}{4\pi j\omega\epsilon_0} \left([M^\phi]^T[G][M^\phi] + [K]^T[G][M^\phi] + [M^\phi]^T[G][K]\right)$$
$$+ \frac{j\omega\mu_0}{4\pi} \sum_{\gamma=x,y,z} [M^\gamma]^T[G][M^\gamma] \tag{9.13}$$

where $[G]$ are the samples of the Greens function over the grid, $[M^\phi]$ are the projections of the divergences of the basis functions onto the interpolating polynomials, $[M^\gamma]$ $(\gamma = x, y, z)$ the vector components also projected on the polynomials and $[K]$ are the projections related to the functions on the triangle contours.

The approximation $[Z^P]$ becomes a poor approximation of the original system matrix when the Lagrange interpolation is performed in proximity of the singularity of the Greens function. In that case a correction is added, a sparse matrix that uses the exact calculation of Z_{mn} if the elements are in the same or adjacent interpolation subdomains.

The wire-like elements in this case are actually normal components on the edge of cell basis functions, there are not independent elements, and there is not a current discretization in that segments. The actual value in those sections are related to the discontinuity on the basis functions even if are modelled as wires in this section.

The implemented solver is integrated with an appropriate preconditioner to allow an efficient analysis, in terms of computational time and memory requirements, of realistic and topologically complex geometries.

Chapter 10

H-refinement

Adaptive h refinement changes the size of elements locally and usually produces a finer mesh. The goal of this work is to obtain a tool that automaticaly decides where a h-refinment is needed, looking for a better description of the current on the object surface. This decision is based on a error estimation obtained for each cell. The selected cells are divided into new cells, and a new problem must be solved.

As input the initial mesh and the error threshold are required. The initial mesh should be only defined by the object geometry, the electromagnetic requirements (more unknowns where the current variation is higher) will be satisfied trough the h-refinement.

10.1   Why Discontinuous Galerkin?

Localized mesh refinement results in a non conformal surface discretization, even if the initial discretization is conformal. If one of two adjacent triangles is not divided due to refined, the common edge will become a boundaru of non-conformity as seen in figure 10.1. The non-conformity is added with each new refinement level.

The standard surface integral equation method can not deal with this non-conformity, and a method with this feature is needed. In the previous chapter the Surface Integral Equation Discontinuous Galerkin scheme has been introduced: interior penalty conditions are inserted in the impedance matrix calculation in order to cancel out the charge accumulation on the mesh edges, as consequence of the non-conformal mesh and the cell-based basis functions.

As the discontinous Glaekin approach is used, the initial mesh conditions can be extended to non-conformal meshes due to geometric reasons, giving extra flexibility
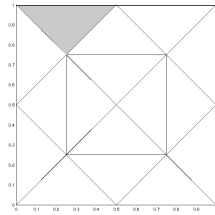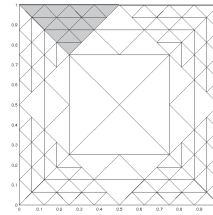
(a) Initial mesh (Conformal) (b) Final mesh (Non-conformal)

Figure 10.1: Localized refinement

to the tool.

In the present work the non-conformity is only related to the different levels of refinement on each mesh cells.

10.2   h-refinement Workflow.

The automatic h-refinemet will start from a geometric mesh and a incidence field conditions (frequancy, direction, etc...) The tool will give at the end a refined mesh with a current solution on it that will satisfy the error requirements decided by the user.

The first step in the automatic process is to obtain an initial current solution on the initial mesh. This mesh has no special requirements in the electromagnetic conditions, it must only described properly the geometry. The solution is obtained by surface integral equation and the obtained current will be used in the next step.

From the found current is possible to estimate current error on the surface. It is calculated as difference from the field generated by the current and the incidence (forced) field. The error information is available in each mesh cell, making possible to select them using the error criteria.

The user will define a threshold to the error. As the error is localized is possible to visualize its behaviour in the surface, and use this information to the selection of the triangles to be refined. The selected triangles are divided (dyadic division). Each triangle becomes 4 new triangles (fig. 10.2). In the case of more levels of refinement each original triangle can be divided in 4, 16, 64 or more triangles, dividing the new created before launch a new solution of the system (figure 10.1 shows a multilevel h-refinement). Could be also possible not to divide all the new triangles, but only

some of them.
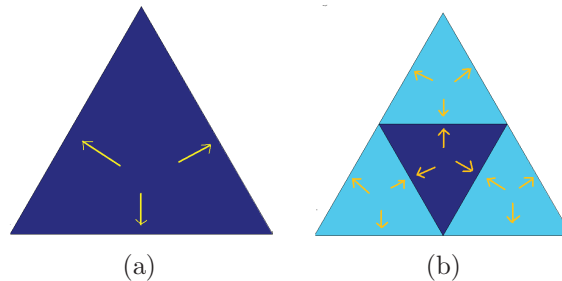
Figure 10.2: Dyadic division. New functions.

The resulting mesh after the h-refinement is a non-conformal mesh. The solution of the new problem is done with the Discontinous Galerkin approach. A new current is obtained, with a better description in the regions where refinement is done.

The new current could be used to estimate the error and discover where on the surface the error current is still higher that the wanted value. In the case of having still some triangles to refine further, the previous steps are repeated. If a multilevel h-refinement is done, is possible to obtain the wanted error in a single iteration.

The process is described in figure 10.3. The error on the initial mesh is estimated (fig. 10.3a) and the triangles to be refined selected (fig. 10.3b). The one-level of the dyadic division generates the mesh in figure 10.3c. The process is depicted again in figures 10.3a, 10.3a and 10.3a starting from the refined mesh of the previous step, estimating the error and producing a new refined mesh after select the triangles with high error.

10.3   Basis Functions.

The non-conformity mesh results in the use of cell-based basis function instead of the edge-based basis function. The cell-based basis function used to describe the current are the half-RWG. These functions are defined as the well-known RWG described in [1], but taking into acount only one of the two triagles. So, a edge-based RWG basis function becomes a cell-based considering only the half.

(a) Initial Error.

(b) Triangles to be refined.

(c) h-refinement.

(d) New error.

(e) Triangles to be refined.
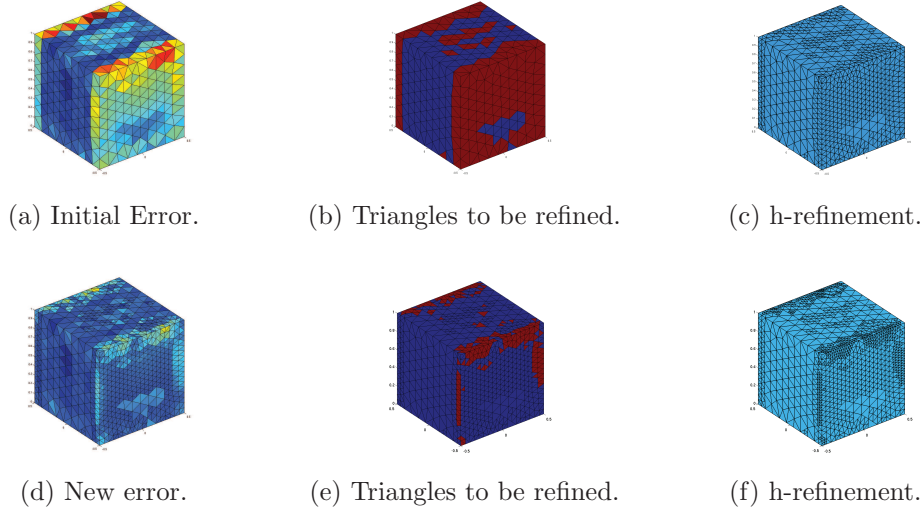
(f) h-refinement.

Figure 10.3: Automatic h-refinement workflow.

The new basis function is defined as

$$\mathbf{f_n}(\mathbf{r}) = \begin{cases} \dfrac{l_n}{2A_n}\rho_n & \mathbf{r} \text{ in } T_n \\ \mathbf{0} & \text{otherwise} \end{cases} \tag{10.1}$$

where l_n is the length of the edge and A_n is the area of triangle T_n. ρ_n is the position vector defined with respect to the free vertex of T_n.

The function has no component normal to the edges where is not defined, hence no line charges exist along these edges. Across the edge where the function is supported the normal component is constant and continous, this component would imply a line charge. The elimination of this charge is the issue solved with the Discontinous Galerkin method.

The surface divergence of $\mathbf{f_n}$, which is proportional to the surface charge density associated with the basis element is

$$\nabla_s \mathbf{f_n}(\mathbf{r}) = \begin{cases} \dfrac{l_n}{A_n} & \mathbf{r} \text{ in } T_n \\ \mathbf{0} & \text{otherwise} \end{cases} \tag{10.2}$$

Thecharge density is thus constant in each triangle.

With this definition of half-RWG basis functions, each triangle is support for three half-RWG basis functions, one related to each edge (fig. 10.2a).

The h-refinement is obtained as dyadic division of each triangle, so the half-RWG basis functions can be used in each new level, giving as result modularity (fig. 10.2b).

Intermesh relationship.

The functions of the coarse level can be exactly described as linear combination of the 12 new functions defined in the 4 triangles after the dyadic division. In [5] this exact relationship is demostrated for RWG, the relationship is developed in this work for the half-RWG.

Each triangle is divided in 4 new triangles halving the edges. The area of the total triangle, A_T, will be the sum of the areas of all the new triangles ($A_T = A_1 + A_2 + A_3 + A_4$) and the edge l is equal to $l_4 + l_5$ (see fig. 10.4a).

(a) Inter-mesh geometry   (b) Reconstructed half-RWG (c) Reconstructed half-RWG on non-conformal

Figure 10.4: Inter-mesh reconstruction of a half-RWG
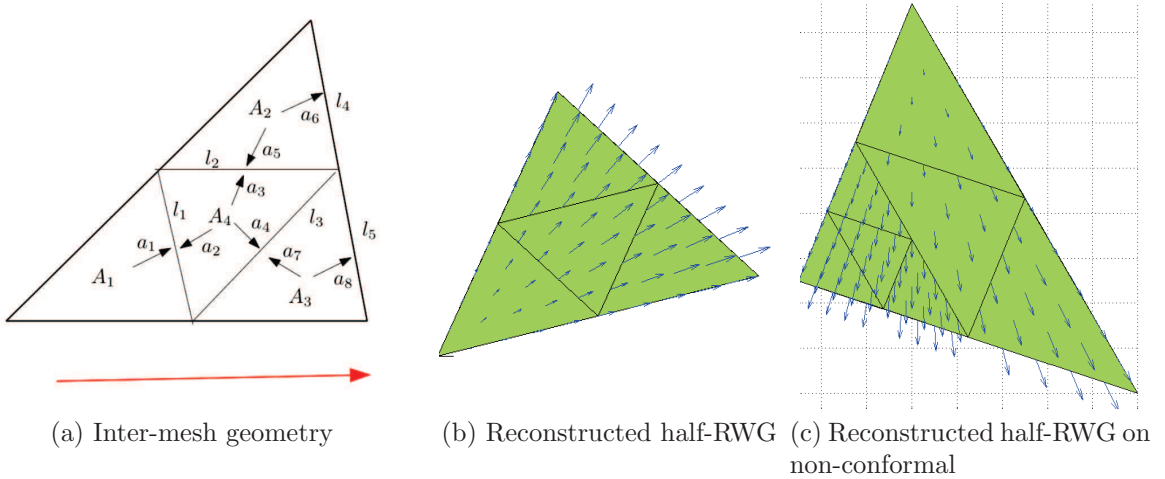
Each half-RWG on the coarse level is the reconstructed from the combination of 9 of the 12 half-RWG of the finer level (the other 3 will not be necessary to describe the half-RWG because are defined in the other edges where there is not normal component of the reconstructed basis function).

The solution of the following system, with a_n the unknowns, gives the description

of the basis function in the coarse level in terms of the half-RWG in the finer level

$$\begin{cases} \dfrac{l}{A_T} = a_1 \dfrac{l}{A_1} \\ \dfrac{l}{A_T} = a_5 \dfrac{l_2}{A_2} + a_6 \dfrac{l_4}{A_2} \\ \dfrac{l}{A_T} = a_7 \dfrac{l_3}{A_3} + a_8 \dfrac{l_5}{A_3} \\ \dfrac{l}{A_T} = a_2 \dfrac{l_1}{A_4} + a_3 \dfrac{l_2}{A_4} + a_4 \frac{l_3}{A_4} \end{cases} \tag{10.3}$$

In [5] each half of the reconstructed RWG is described by RWGs, so we can impose $a_2 = -a_1$, $a_5 = -a_3$ and $a_7 = -a_4$. A possible solution to the linear system is

$$\begin{cases} a_1 = \dfrac{lA_1}{A_T l_1} \\ a_3 = \left(\dfrac{l}{A_T} + \dfrac{l_1 a_1}{A_4} \right) \dfrac{A_4}{l_3(2)} \\ a_8 = \left(\dfrac{l}{A_T} + \dfrac{a_3 l_3}{A_2} \right) \dfrac{A_2}{l_4} \\ a_6 = \left(\dfrac{l}{A_T} + \dfrac{l_3 a_3}{A_3} \right) \dfrac{A_3}{l_5} \\ a_4 = a_3 \dfrac{l_3}{l_2} \end{cases} \tag{10.4}$$

Is possible only to keep the new functions, this set is a new base to the problem, but is also possible to pass from a level to another using the coefficients defined in eq. 10.4.

Chapter 11

Local Error Estimation

An automatic local refinement needs to know how the error is on the interest surface to decide where the triangle division is wanted. A global error is not useful to perform the localized refinement, because the idea is to know where in the object the variation of current is not properly described by the available basis functions.

The unavailability of "exact" or correct current description for general objects makes necessary the *prediction* of the error based on the information of the incident field and the solution instead of the error *calculation*. Exact solutions are available only for some canonical surfaces, but in general the prediction of the error is the remaining option.

In the following sections a error estimation is proposed. The current obtained of the solution of an electromagnetic problem is used with high-orders basis functions to estimate how much the solution is far from the exact values.

11.1   Error current

The error current is the diference between the scattered field produced by the current on the object and the incident electromagnetic field, both calculated on the surface Γ. In the following this current will be $\mathbf{M}^{\mathbf{err}}$, and is equal to

$$\mathbf{M}^{\mathbf{err}} = L\{\mathbf{J}\} - \mathbf{n} \times \mathbf{E}^{\mathbf{inc}} \tag{11.1}$$

where the L operator is the electic field operator

$$L\{\mathbf{J}\} = j\eta\hat{\mathbf{n}} \times \left(\int_\Gamma \frac{e^{-jk|x-x'|}}{4\pi|x-x'|}\mathbf{J}(x')dx' - \frac{1}{k}\nabla \int_\Gamma \frac{e^{-jk|x-x'|}}{4\pi|x-x'|}\nabla \cdot \mathbf{J}(x')dx' \right) \tag{11.2}$$

The definition of $\mathbf{M^{err}}$ is similar to the definition of EFIE residual $\mathbf{R}^{(E)}$ on section 9. The problem was then to find a current $\mathbf{J}$ such that residual was equal to 0.

$$\mathbf{J} = \sum_{i=1}^{N} I_i \mathbf{f_i} = \tilde{\mathbf{I}}^T \tilde{\mathbf{f}} \qquad (11.3)$$

where $\tilde{\mathbf{f}}$ are the electric current basis functions, typically RWG functions for the conforming mesh.

A result current $\mathbf{J}(x)$ is found when the EFIE system is solved. This current J is the one that describes best the true solution on the particular space defined by the chosen basis functions. Still the error current $\mathbf{M^{err}}$ can be used to know how this solution is close to the continuos current (true solution) and, in the the particular case of the h-refinement, where is possible to improve the solution.

11.2 Error estimation

As the true solution is unknown, the error current $\mathbf{M^{err}}$ presented in the previous section can be used to find how the current is different from the actual one. The error e is defined as

$$e = \|\mathbf{M^{err}}\| \qquad (11.4)$$

The norm of $\mathbf{M^{err}}$ is not easy to obtain because the hypersingularity in the second term of $L\{\mathbf{J}\}$ (equation 11.2) makes difficult to integrate the square of this term. The norm can be approximated using a projection on a space V of testing functions.

The norm is approximated as

$$\|\mathbf{M^{err}}\| \approx \|\mathbf{M^{err}}\|_V = max_{\mathbf{j^{(2)}} \in V} \frac{\langle \mathbf{M}, \mathbf{j^{(2)}} \rangle}{\sqrt{\langle \mathbf{j^{(2)}}, \mathbf{j^{(2)}} \rangle}} \qquad (11.5)$$

This approximation approaches the true norm as V approaches the continuous space [6].

In the solution of the Surface Integral Equation the main goal is to make $\mathbf{M^{err}}$ orthogonal to the basis function space (RWG function space usually). Practically this can not be completely achieved and theres is a contribution form the basis functions to $\mathbf{M^{err}}$ in the order of the solver tolerance. This contribution can be

65

approximated to zero by testing the error current with the next higher order basis functions

The purpose of the EFIE is to make $\mathbf{M^{err}}$ orthogonal to the RWG function space. In practice this can not be completely achieved and there is a contribution from the RWG functions to $\mathbf{M^{err}}$ that is of the order of the solver tolerance. This contribution can be approximated to zero by testing with only the next higher order basis functions.

Seen in other way: $\mathbf{M^{err}}$ is projected onto the higher-order basis and the L_2 norm of the result is calculated. Is expected that the error in the current will be in a higher order space of basis functions, because the solution of the linear system in the low-order basis functions spaces makes zero the error on that space, as is imposed in the problem formulation, in the cancellation of the residues.

The definition of $\mathbf{M^{err}}$ can be made in each cell, as the projection of it onto a higher order function space V, it gives an advantage used in the localized h-refinement: the error can be evaluated numerically at any point on the scatterer's surface.

11.3   Implementation

The norm calculation of $\mathbf{M^{err}}$ in the definition of e will be approximated with the projection of it on a function space V as said in previous section. This projections leads to the application of the inner product between $\mathbf{M^{err}}$ and the basis functions $\mathbf{j^{(2)}}$.

The inner product $\langle \mathbf{M^{err}}, \mathbf{j^{(2)}} \rangle$ becomes, following the definition of $\mathbf{M^{err}}$ given in (11.1), the testing of the difference between scattered field and incident field with the higher order basis functions as

$$\langle \mathbf{M^{err}}, \mathbf{j^{(2)}} \rangle = \langle L\{\mathbf{J}\} - \mathbf{\hat{n}} \times \mathbf{E^{inc}}, \mathbf{j^{(2)}} \rangle \tag{11.6}$$

This inner product can be, by linearity, written as the inner product of each term in the subtraction, as

$$\langle \mathbf{M^{err}}, \mathbf{j^{(2)}} \rangle = \langle L\{\mathbf{J}\}, \mathbf{j^{(2)}} \rangle - \langle \mathbf{\hat{n}} \times \mathbf{E^{inc}}, \mathbf{j^{(2)}} \rangle \tag{11.7}$$

In the case in discussion in this work $\mathbf{j^{(2)}}$ is a higher order basis function. In (11.3) we defined $\mathbf{J}$ as linear combination of the N basis functions defined in Γ,

being $\mathbf{J}$ the current solution on the Γ surface.

If we use M higher order basis functions $\mathbf{j^{(2)}}$, in corrispondence with the basis functions used to describe the current, we have a system very similar to the matrix linear system defined before as result of the Galerkin (or Discontinous Galerkin method). The difference is that higher order basis function ($\mathbf{j^{(2)}}$) are used for testing, instead of the same low-order basis function ($\mathbf{f}$).

The $\mathbf{j^{(2)}}$ higher order basis functions used in this implementation are defined in [7].

Following these considerations, we start from the current discretization in the basis function space $\mathbf{f}$ as

$$\mathbf{J} = \sum_{i=1}^{N} I_i \mathbf{f_i} = \tilde{\mathbf{I}}^T \tilde{\mathbf{f}} \tag{11.8}$$

The projection $\langle \mathbf{M}, \mathbf{j_j^{(2)}} \rangle$ can be presented as

$$\langle \mathbf{M}, \mathbf{j_j^{(2)}} \rangle = Z_t \tilde{\mathbf{I}} - \mathbf{v_{j^{(2)}}} \tag{11.9}$$

In equation 11.9 the new known term $\mathbf{v_{j_j^{(2)}}}$ is introduced, the name is given by similarity with the usual Method of Moments nomenclature. This term is defined as $\mathbf{v_{j_j^{(2)}}} = \langle \hat{\mathbf{n}} \times \mathbf{E^{inc}}, \mathbf{j_j^{(2)}} \rangle$, with coefficients vector $\tilde{\mathbf{I}}$.

Following with the similarity with the standard Metohd of Moments, the matrix Z_e is defined as

$$Z_e(i,j) = \langle L\{\mathbf{f_i}\}, \mathbf{j_j^{(2)}} \rangle \tag{11.10}$$

It is equivalent to calculate a impedance matrix where the testing functions are not the source functions (Galerkin method), but the higher order basis functions. The number of higher order basis functions in a cell is higher than the number of lower order, so the matrix Z_e is not a square matrix. It has dimensions M×N where N is the total number of basis functions used to describe the current, and M the total number of basis functions of high order defined on the same surface.

Chapter 12

Numerical results

In this chapter, some automatic h-refinement cases are presented and discussed. The automatic h-refinement tool proposed in previous chapter has been implemented and tested. A Discontinous Galerkin Method is used to solve the issue of the non-conformity in the mesh (non continuity of the trial space functions) resulted of the refinement. All together gives an error adaptative mesh as seen in the following sections.

12.1   Simple Test Case

For the very first test case a cube is used. The edges of the cube permit to observe the error in the current. The current in the edges has a high variation, respect to the other regions of the body. It implies that more basis functions are required to describe properly the current. The identification of these regions is the goal of the refinement tool.

The cube is 2 λ side, simulated at 600 MHz and with incidence from $+z$. Figure 12.1 depicts the current in a very fine mesh, that could be used as reference. This case permit the calculation of a reference solution, because its dimensions.

The cube is discretized with a coarse mesh ($\lambda/5$ i.e.), this initial mesh is depicted in fig. 12.2a. The following meshes are obtained in two ways. Figure 12.2b shows the mesh obtained by automatic h-refinement, depending on the error of the initial mesh (fig. 12.3a), that is crearly a non-conforming mesh. The uniform refinement (dyadic division of all triangles) is the one of figure 12.2a, that mantains the conformity in the mesh.
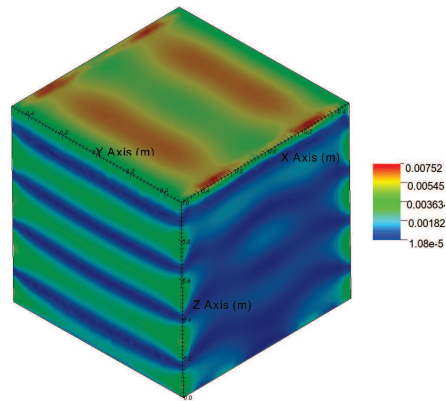
Figure 12.1: Reference Current

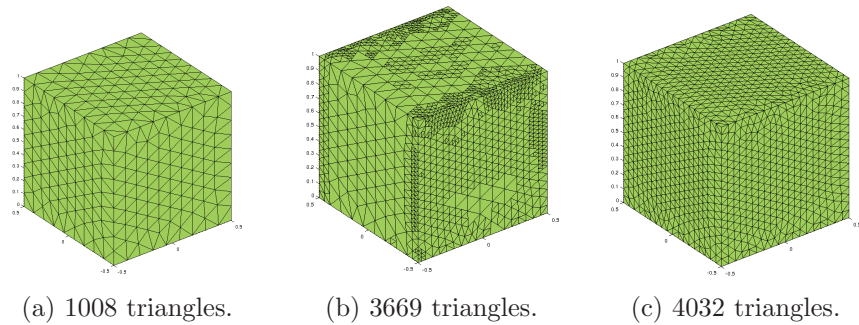(a) 1008 triangles.   (b) 3669 triangles.   (c) 4032 triangles.

Figure 12.2: Mesh for refinement

The error is estimated on the initial mesh (fig. 12.3a). Using the automatic h-refinement tool, and the user-defined error threshold (0.01), is possible to estimate the error of this refined mesh (figure 12.3b). The initial mesh had 1008 triangles, 51 % of which were above the threshold. After h-refinement only 1 % of the 3669 triangles have and error above the wanted by the user.

The uniform refinement has a distribution of error with 11 % of the triangles above the threshold, using 4032 cells. So, with almost the same quantity of triangles (10 % less, in fact), the surface above error pass from 11 % to 1 %. Also the maximun error is improved: passes from 0.323 in the initial mesh to 0.014 in the h-refined, instead of 0.02 of the uniform refinement.

As said before, a reference case could be possible for this particular object. A $\lambda/80$ conformal mesh is obtained, and the current defined on it is considered as the

(a) 51% above error threshold (b) 1% above error threshold (c) 11% above error threshold (d) Scale
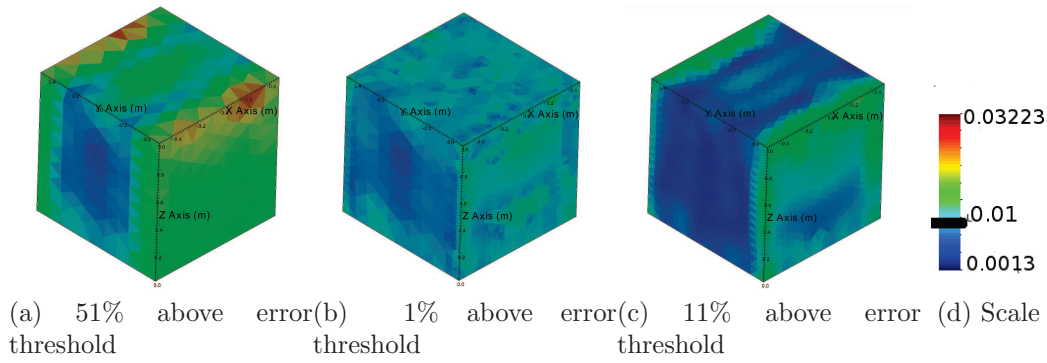
Figure 12.3: Current error on refined body.

reference one. A current error can be obtained as difference between the current description obtained in each case and the reference one tha had been just defined.

Continuing with the automatic and uniform refinement, the comparison in figure 12.4 shows up how the first can give better results. An error of 1e-6 is obtained by the h-refined mesh (black line) with less triangles than the $\lambda/20$ case (green line). If the goal error is wanted with the uniform refinement starting from the $\lambda/20$ mesh, the quantity of triangles must be multiplied by four ($\lambda/40$ mesh - red light). The current error in all the structure is achieved by using the h-refinement with a quarter of the numer of triangles than the uniform refinement.
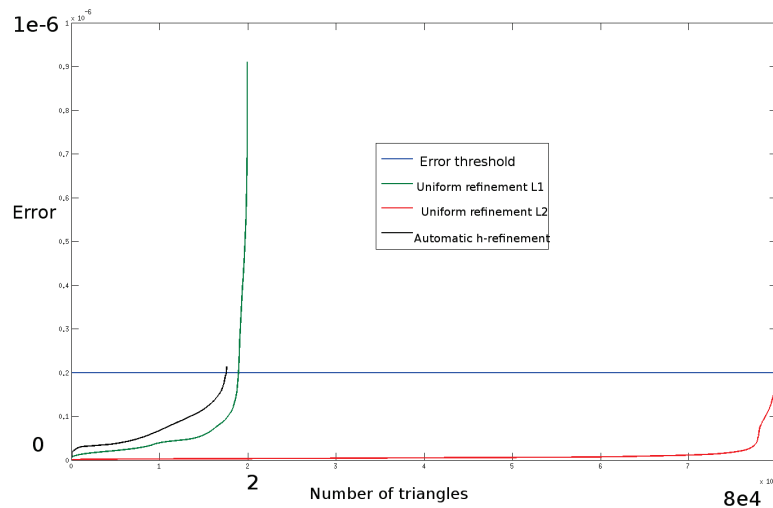

Figure 12.4: Error in triangles.

70

The cube is a particular case with edges in all the sides. A real case with smooth surfaces but with some sharp edges or details, might require the h-refinement in very particular and small zones, giving either better performance than the one here presented.

From the current distribution in figure 12.1 is possible to conclude that if the incidence of the field changes, also the regions where the variation is high, and as consequence the selection of triangles to be refined. This permits that not only the geometrical information defines the refinement, but also the electromagnetic information, avoiding, for example, to refine triangles in a sharp edge where the current is close to zero.

12.2   Satellite at 500 MHz

The second test case is a real object. In this case a satellite body is used. The cube form of the satellite remembers the characteristics of the simple cube: big regions with small variation in current and sharp edges where the variation is high. Added to those properties, some details due to the geometry and to the antenna reflectors and devices are present.

The main goal of this test is to show how the error distribution depends on the details, and how the error is reduced to a defined treshhold using the automatic h-refinement tool.

Figure 12.5a depicts the current on a test object using a frequency of 500 MHz. The mesh size of this initial $\lambda/5$. The error estimator is used and, as expected, error is greater close to sharp edges and to small details (fig. 12.5b). Using the cell-based information of the error, and fixing a deliberately high threshold, some triangles in the mesh are selected to be refined (fig. 12.5c).

The new problem is solved (fig. 12.6a), the current in this case should be closer to the real solution. A new estimation of the error (fig. 12.6b) confirms the decrease in the error on the surface (the distribution is more uniform) and the maximum passed from 0.238 to 0.12 (the wanted threshold). The threshold is not achieve in all the selected triangles, because in some cases a subsequent division should be necessary in one of the new triangles, because the current variation is still high. To the next step of refinement a new threshold is fixed (0.02) to select the triangles to be refined (fig. 12.6c).
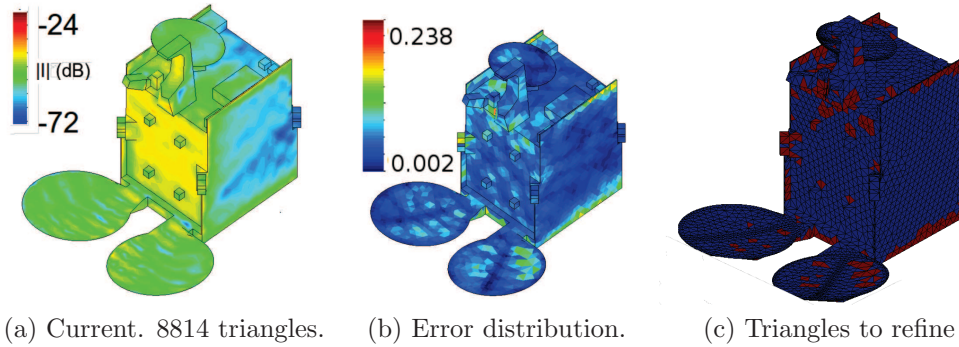
(a) Current. 8814 triangles.   (b) Error distribution.   (c) Triangles to refine

Figure 12.5: Step 1. Max error = 0.238. Threshold = 0.1

(a) Current. 9504 triangles.   (b) Error distribution.   (c) Triangles to refine
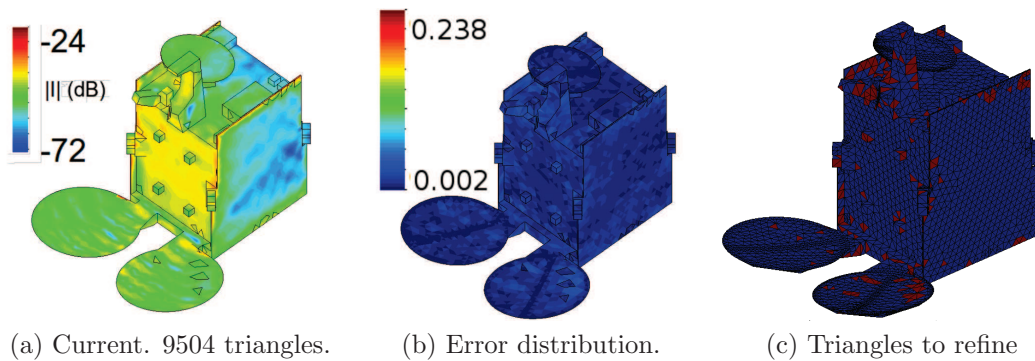
Figure 12.6: Step 2. Max error = 0.12. Threshold = 0.02

The solution of the third refined mesh is presented in figure 12.7a. The error of this current is depicted in figure 12.7b. The maximum error is close to the defined threshold, but some triangles may be above that level as explained before, a new refinement with the same threshold could eliminate them. The quantity of triangles is almost the 30 % more than the original mesh, but the maximum error on the surface has dcreased in two orders of magnitude.

In this case the final solution has been obtained after 3 iterations, but could be interesting to set the triangles to be refined and the total levels of the refinement from the begining to achieve the final solution in one-shot simulation. This part is on study, the error can be concentrated in one side of the triangle, for example, so a uniform higher level of refinement on each triangle could not be the optimal solution.
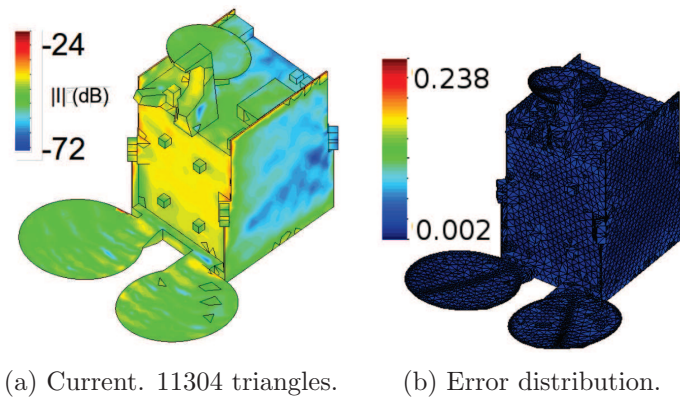
(a) Current. 11304 triangles.   (b) Error distribution.

Figure 12.7: Step 3. Max error = 0.025

Chapter 13

Conclusions and Perspectives

13.1 Conclusions

The present work presents an automatic tool to perform h-refinement depending on error on the structure, starting from a coarse mesh.

A test object can have either smooth regions and detailed parts or edges. The description of the current in the whole object might require a lot of unknowns if an uniform meshing is used, sometimes with a higher number of unknowns in regions where a lower quantity might be used.

The regions where less basis functions to describe the current are needed must be identified. To this task, would be useful know how the current error is distributed in the object surface. The error regarding a "true solution" is not feasible, because this solution is only available in some benchmark cases, or require heavy simulations (high number of unknows) that is exactly the thing that is wanted to avoid.

Instead of the calculation of the current error, is proposed the estimation of a current error on the surface as the difference between the scattered field by the current on study and the incident field. As this difference must be zero in the discretized system of basis functions, it is projected on higher order basis functions.

The process of refinement starts from a coarse mesh, with the only goal of describe correctly the geometry. A first solution of the problem is obtained and the error is estimated. Depending on the error and on a user-defined threshold, the h-refinement is done. The triangles with error above a value are divided (dyadic-division), adding new basis functions that describes better the current variation in that region.

The dyadic division in the triangles only in some of them, drives to a mesh that is not conforming. An common edge to two original triangles could be, after the refinement, between an original triangle and two new ones (or more if the level of refinement is higher).

As the usual surface integral equation is proposed for the continous trial functions (Galerkin Method) present in a conforming mesh, a generalization is needed to include the case of non-conforming meshes. The Discontinous Galerkin method add penalty terms to avoid the accumulation of charge on the edges, accumulation that is result of the non continuity of the definition of the basis functions. Cell-based functions are used and the delta in the edges is considered in the formulation through the penalty terms, forced in weak mode.

One of the advantages of the localized refinement is the option of use information calculated. In the matrix linear system not all the elements must be calculated, but only the ones that involve new triangle elements. The previous current can be used also as initial guess for the solution of the new one: The current on the original triangles would not change (at least in regions far from refined zones) and the basis functions on dyadic division triangles can reconstruct exactly the basis function in the original mesh, bringing a connection between original mesh and new mesh, and between the currents.

In summary, the automatic h-refinement permits the use of more basis functions only in the zones of the surface where is needed, where the error is higher. This drives to problems with less unknowns (less processing time and memory) with a good accuracy.

13.2   Perspectives

The h-refinement introduces a multiscale mesh, it deteriorates the conditioning of matrix system. Is also noticed that the discontinous galerkin approach generates a matrix with poor conditioning, due to the high interaction between functions out of the diagonal (The functions that share an edge, for example).

A multiresolution preconditioner will give a better performance. This preconditioner will have a hierarchical form, easily obtained from the refinement, because each level is related exactly with the previous ones.

Bibliography

[1] S.M. Rao, D. Wilton and A.W. Glisson. *Electromagnetic scattering by surfaces of arbitrary shape* IEEE Transactions on Antennas and Propagation. vol. 30 1982.

[2] Z. Peng, K.-H. Lim and J.-F. Lee. *A Discontinuous Galerkin Surface Integral Equation Method for Electromagnetic Wave Scattering From Nonpenetrable Targets* IEEE Transactions on Antennas and Propagation vol. 61 2013.

[3] M. A. Francavilla, F. Vipiana, G. Vecchi and D. R. Wilton *Hierarchical Fast MoM Solver for the Modeling of Large Multiscale Wire-Surface Structures*, IEEE Antennas and Wireless Propagation Letters, vol. 11, 2012.

[4] S. Seo and J. Lee. *A fast IE-FFT algorithm for solving PEC scattering problems*, IEEE Transactions on Magnetics, vol. 41, may 2005.

[5] F. Vipiana, P. Pirinoli and G. Vecchi. *A Multiresolution Method of Moments for Triangular Meshes*, IEEE Transactions on Antennas and Propagation. vol. 53 no. 7 july 2005.

[6] M.B Stephanson and J.-F. Lee. *Automatic Basis Function Regularization for Integral Equations in the Presence of Ill-Shaped Mesh Elements* IEEE Transactions on Antennas and Propagation vol.61, 2013.

[7] R.D. Graglia, D.R. Wilton and A.F. Peterson. *Higher Order Interpolatory Vector Bases for Computational Electromagnetics*, IEEE Transactions on Antennas and Propagation. vol. 45 no.3, march 1997.

[8] Z. Peng, K.-H. Lim and J.-F. Lee. *Discontinuous Galerkin Integral Equation Method for Time-Harmonic Electromagnetic Problems* 2013 IEEE International Symposium on Antennas and Propagation and USNC/URSI National Radio Science Meeting Orlando, FL, USA. jul 8–13 2013.

[9] F. G. Bogdanov, and R. G. Jobava and S. Frei. *Estimating accuracy of MoM solutions on arbitrary triangulated 3-D geometries based on examination of boundary conditions performance and accurate derivation of scattered fields*, Journal on Elecromagnetic Waves and Applications. vol. 18, no. 7, may 2004.

Acknowledgment